

Probing two-level systems with a surface acoustic wave resonator

Master's thesis in Erasmus Mundus Master of Nanoscience and Nanotechnology

NUTTAMAS TUBSRINUAN

Promoter: Prof. Per Delsing
Co-promoter: Prof. Bart Soree
Supervisor: Gustav Andersson

MASTER'S THESIS IN ERASMUS MUNDUS MASTER OF
NANOSCIENCE AND NANOTECHNOLOGY

**Probing two-level systems with
a surface acoustic wave resonator**

NUTTAMAS TUBSRINUAN



CHALMERS
UNIVERSITY OF TECHNOLOGY

Department of Microtechnology and Nanoscience
Quantum Technology Laboratory
CHALMERS UNIVERSITY OF TECHNOLOGY
Gothenburg, Sweden 2021

Probing two-level systems with a surface acoustic wave resonator
NUTTAMAS TUBSRINUAN

© NUTTAMAS TUBSRINUAN, 2021.

Promoter: Per Delsing, Chalmers University of Technology
Co-promoter: Bart Soree, KU Leuven
Supervisor: Gustav Andersson, Chalmers University of Technology

Master's Thesis 2021
Department of Microtechnology and Nanoscience
Quantum Technology Laboratory
Chalmers University of Technology
SE-412 96 Gothenburg
Telephone +46 31 772 1000

Cover: Correlation coefficients of frequency noises caused by parasitic two-level systems interacting with a surface acoustic wave resonator.

Typeset in L^AT_EX
Printed by Chalmers Reproservice
Gothenburg, Sweden 2021

Probing two-level systems with a surface acoustic wave resonator
NUTTAMAS TUBSRINUAN
Department of Microtechnology and Nanoscience
Quantum Technology Laboratory
Chalmers University of Technology

Abstract

Parasitic two-level systems (TLSs) cause detrimental effects on the performance of superconducting quantum devices. To mitigate this problem, a better physical understanding of the TLS coupling mechanism is crucial. In this thesis, a new approach for probing TLSs using a surface acoustic wave (SAW) resonator is presented. Having a small mode spacing, the SAW resonator enables an investigation of the frequency noises caused by TLSs at many different frequencies simultaneously.

We report a novel result of the correlated frequency noise caused by TLSs. The correlations of the noise diminish with increasing detuning, which is in agreement with the prediction of the TLS model. However, the frequency noises also show negative correlations, which cannot be explained by the current physical model. Additionally, the frequency noise correlation between different modes shows a power and temperature-dependent behavior. Although some previous experiments have reported the power and temperature dependence of the frequency noise spectra, the relationships of the noise at several different frequencies have not been studied. Therefore, further investigations, both experimental and theoretical aspects, of the multifrequency noise beyond this work are required.

Keywords: two-level system, surface acoustic wave, SAW resonator, resonance frequency fluctuation, tunneling model, frequency noise, correlation, frequency comb

Acknowledgments

I would like to express my sincere gratitude to everyone who has supported me to complete this master thesis, especially the following people:

Per Delsing for the opportunity to carry out my master project at the Quantum Technology laboratory and for his supervision and helpful feedback throughout this project.

Gustav Andersson, my daily supervisor, for his valuable suggestions, countless discussions, patience, relentless support, and encouragement whenever I need it.

Bart Soree, my co-promoter and the program director of EMM Nano, for the internship opportunity with the quantum computing group at imec and co-promoting this project.

Jared H. Cole and Jonathan Burnett for their insightful suggestions about the experiment and the two-level system discussions.

Anton Potočnik, my internship supervisor at imec, where I got the first chance to do research in quantum computing and learn about the parasitic two-level systems.

Bart Raes and Joris Van de Vondel, my project work supervisors, for the great supervision and the opportunity to do research at the Quantum Solid-State Physics laboratory at KU Leuven. The knowledge and experience I gained from working with them have helped me a lot to carry out this master project.

Shuangyue Yang, my best friend, who nurtured and supported me throughout a difficult time in Leuven.

Karel Joos, Arno van Dingenen, Michiel Schroven, Anne Ascard, and Kristina Fahlén for listening to my problems and giving many useful pieces of advice.

My EMM Nano fellas for a friendly and stimulating environment.

Thilo Bauch and Elke Delfost, for all assistance during the entire study program.

The European Commission for the prestigious Erasmus Mundus scholarship in this master of nanoscience and nanotechnology.

Finally, I would like to express my deepest appreciation to my parents, my sister, and my family for understanding and unconditional support.

Nuttamas (Pias) Tubsrinuan
Gothenburg, Sweden
August, 2020

Contents

List of Figures	xi
1 Introduction	1
2 Theory	3
2.1 Two-level system	3
2.2 Surface acoustic wave resonator	6
2.3 Lock-in amplifier	7
2.4 Frequency mixer	7
3 Methods	11
3.1 Experimental setup	11
3.1.1 SAW resonator	11
3.1.2 Multi-frequency lock-in amplifier	11
3.1.3 Frequency conversion	12
3.1.4 Measurement configuration	12
3.2 SAW resonator characterization	12
3.3 Normalizing the number of phonons in the resonator	14
3.4 Phase noise measurement	15
3.5 Resonance frequency calculation	16
3.6 Data analysis	17
3.6.1 Welch power spectral density	17
3.6.2 Allan deviation	17
3.6.3 Correlation coefficient	18
3.6.4 Magnitude-squared coherence	18
4 Results and discussion	21
4.1 SAW resonator profile	21
4.2 Investigating the noise caused by TLSs	21
4.2.1 Noise process identification	22
4.2.1.1 Noise power spectral density	23
4.2.1.2 Allan deviation	23
4.2.2 Correlations of the resonance frequency fluctuations	24
4.2.2.1 Correlation coefficients	24
4.2.2.2 Magnitude-squared coherence	25
4.2.3 Power dependence of the resonance frequency shifts	25
4.2.4 Temperature dependence of the resonance frequency shifts	27

4.3 Exploring the local effects of the TLSs	27
5 Conclusion	35
Bibliography	37
A MLA setup	I
A.1 Intermodulation software	I
A.2 MLA setup	I
B Scripts for measurements	III
B.1 Frequency sweeping	III
B.2 Amplitude optimization	V
B.3 Phase noise measurement	VII
C Supplementary data	XI
C.1 Long measurement	XI
C.2 Single-mode measurement	XII

List of Figures

2.1	(Left) an illustration of the formation of TLS and (right) the double-well potential.	4
2.2	(a) an interdigital transducer (IDT) in operation and (b) a one-port SAW resonator.	6
2.3	Amplitude and phase response of a SAW resonator as a function of frequency in three different coupling regimes: (top) overcoupled, (middle) critically coupled, and (bottom) undercoupled. The red crosses represent amplitude and phase response at the resonance frequency.	8
2.4	Frequency mixer basic operation	9
3.1	The SAW resonator used in this study [10].	12
3.2	A diagram illustrating the SAW resonator installed in a dilution refrigerator.	13
3.3	A circuit diagram representing the experiment setup. The LO pumps a GHz signal. The MLA generates a multifrequency signal to be up-converted by the up-conversion mixer. The signal is up-converted to the GHz range. The up-converted signal is sent to the SAW device. The reflected signal goes to the bandpass filter and the room temperature amplifier before being down-converted by the down-conversion mixer. Finally, the down-converted signal is read by the MLA.	14
3.4	Amplitude and phase response of the SAW resonator, measured in reflection at input power -47 dBm.	15
4.1	Amplitude and phase responses of a the SAW resonator response at input power (top) -47 dBm, (middle) -57 dBm, and (bottom) -67 dBm. The blue text indicates the mode index, which will be referred to in the following discussions.	22
4.2	(Top) the loaded quality factors Q_L , (middle) the external quality factors Q_C , and (bottom) the internal quality factors Q_i of the SAW resonator at each frequency when using different input powers.	23
4.3	The time traces of the measured phases. The bottom trace represents the control tone measured at 2.39 GHz, which is off-resonance with the SAW modes.	24
4.4	The time trace of the calculated resonance frequency shifts calculated using Equation 3.10. The time trace of the calculated resonance frequency shifts. Note that there is no converted frequency from the control tone because it does not correspond to any resonance mode.	25

4.5	Welch power spectral density (S_y) of the resonance frequency fluctuation Δf_r . Note that only mode #1, #8 and #14 are displayed. The fitted functions are fitted to mode #8.	26
4.6	Allan deviation of the resonance frequency f_r . The peaks indicate the presence of a single dominant TLS, which dominates in time period of 1 - 10 s.	27
4.7	(Left) The matrix showing the correlation coefficients of phase and (right) the resonance frequency shifts.	28
4.8	The correlation coefficients of resonance frequency shift, Δf_r , as a function of detuning. Note that all the data seem to collapse to a single line. Also, note the change in sign when the detuning is about ± 18 MHz.	29
4.9	Magnitude-squared coherence of the resonance frequency shift Δf_r between mode #1 and (top) mode #2, (middle) mode #11, and (bottom) mode #14.	29
4.10	The power dependence of the frequency noise from mode #8 at the temperature of 10 mK.	30
4.11	The correlation coefficients of the resonance frequency shifts derived from (top left) mode #1, (top right) mode 5, (bottom left) mode #10 and (bottom right) mode #14 with the other modes as a function of estimated number of phonons $\langle N \rangle$ and detuning.	30
4.12	An example of Welch power spectral density of Δf_r of mode #8 at different temperatures.	31
4.13	Temperature dependent of the frequency noise from mode #7 to #9. The data are fitted to $S_y \sim T^{-(1+\mu)}$. We get $\mu = \{0.28, 0.32, 0.23\}$ for mode #7, #8, #9, respectively.	31
4.14	The correlation coefficients of the resonance frequency shifts derived from (top left) mode #1, (top right) mode #5, (bottom left) mode #10 and (bottom right) mode #14 with the other modes as a function of temperature and detuning.	32
4.15	The correlation coefficients of the resonance frequency shifts as a function of detuning when driving different number of tones in the SAW resonator.	33
C.1	The time traces of the measured amplitudes. The bottom trace represents the control tone measured at 2.39 GHz, which is off-resonance with the SAW modes.	XI
C.2	The time traces of the measured phases. The bottom trace represents the control tone measured at 2.39 GHz, which is off-resonance with the SAW modes.	XII
C.3	The time trace of the calculated resonance frequency shifts. Note that there is no converted frequency from the control tone because it does not correspond to any resonance mode.	XIII
C.4	(Left) Welch power spectral density and (right) Allan deviation of the resonance frequency shifts.	XIII

C.5	The correlation matrices of (left) the amplitudes and (right) the phases of the data.	XIV
C.6	(Left) the correlation matrices of the resonance frequency shifts and (right) the plot showing correlation coefficients as a function of detuning.	XIV
C.7	Magnitude-squared coherence of the resonance frequency shifts between mode #1 and the others.	XV
C.8	The probing frequencies driven in a single mode measurement.	XVI
C.9	The matrices showing correlation coefficients of (left) the amplitudes and (right) the phases of the single mode measurement.	XVI
C.10	The matrices showing correlation coefficients of the resonance frequency shifts calculated from the single mode measurement.	XVII

1

Introduction

Quantum computers show high potential to overcome the computational limit of classical computers and offer computing power beyond state-of-the-art technology [1]. To implement the concept of quantum computing, a reliable fundamental unit of information (a qubit) must be achieved. One of the proposed candidates for a qubit that is promising for the transfer from the research field towards real applications is the superconducting qubit. Despite having the advantages of scalability and compatibility with the existing microwave control systems, the energy loss in a superconducting quantum circuit due to the coupling with parasitic two-level systems (TLSs) remains unsolved. This is one of the main factors that limits the coherence time of a superconducting qubit [2].

Although the understanding of the nature of the TLS is not comprehensive, it is known that there two types of TLSs, namely coherent TLSs and thermal fluctuators. The interaction between coherent TLSs and thermal (incoherent) fluctuators gives rise to TLS energy drift [3]. At the same time, the coherent TLSs dispersively couple with a qubit, leading to the fluctuations of the qubit resonance frequency [4]. This time-dependent resonance frequency shift shows a $1/f$ spectrum, which has been observed in both superconducting qubits [2] and microwave resonators [3, 5]. Surface acoustic wave (SAW) devices have been emerging in the quantum device research field [6, 7, 8]. Manenti *et al.* [9] have shown the evidence that the losses in a SAW resonator at cryogenic temperatures are partly caused by the device coupling with TLSs. In the later experiment by Andersson *et al.*, TLSs were shown to dominate the losses [10]. Since an electromagnetic wave travels in a microwave circuit with a velocity slightly lower than 3×10^8 m/s, a microwave resonator has a large mode spacing, which restricts experiments only a few frequencies. In contrast, the velocity of a sound wave is approximately 3×10^3 m/s. As a consequence, the spacing between modes is smaller, enabling the study of the TLS coupling between many different modes.

Using a SAW resonator, we can probe TLSs at many frequencies simultaneously. Investigating the correlation of the resonance frequency fluctuation between different modes could lead to a better understanding of the TLS coupling mechanism. An insight into the TLS nature could support the development of a superconducting quantum computer, e.g. suggest how often to perform qubit calibration and, potentially, a method to mitigate the loss due to the qubit coupling with the TLSs.

In this thesis, the theoretical background of TLSs and the physics of the experiment are explained in Chapter 2. Chapter 3 describes the experimental setup, data acquisition, and analysis methods. Chapter 4 demonstrates how data are analyzed and interpreted, as well as discusses the results. Finally, Chapter 5 summarizes the

1. Introduction

project and conveys some ideas for future work.

2

Theory

This chapter provides the theoretical background of each element for readers to understand the work done in this thesis. Section 2.1 briefly describes the physics of two-level systems (TLSs) and their impacts on a superconducting qubit and a resonator. Section 2.2 introduces a surface acoustic wave (SAW) resonator and explains its advantage over a microwave resonator for studying the correlations of resonance frequency fluctuations between different modes. To investigate the resonance frequency shift, we measure phase noise by pumping a multi-frequency signal and measuring reflection coefficients of a SAW resonator. The measurement requires a frequency mixer and a lock-in amplifier. Their working principles are explained in sections 2.3 and 2.4.

2.1 Two-level system

Two-level system (TLS) is a term referring to a defect that is the main source of noise and decoherence in superconducting quantum devices [4]. One of the models proposed to explain the origin and the behavior of TLSs is the standard tunneling model (STM) [11, 12]. According to the STM, TLSs arise from dangling bonds, tunneling of single atoms, or a small group of atoms that moves between two potential minima in amorphous materials [4]. TLSs can couple both with an electromagnetic field [13, 14] and a strain field [15, 16], allowing the transition between a ground state and an excited state. The energy landscape of the TLS is described by a double-well potential. At very low temperatures, a thermal excitation over the barrier is limited. Therefore, the dynamics of the TLS is dominated by a tunneling process. An illustration of the TLS origins and a model of its energy landscape are shown in Figure 2.1. The energy associated with tunneling is described by Δ_0 . The energy asymmetry of the wells, assumed to be uniformly distributed, is represented by a parameter ϵ . The Hamiltonian of an individual TLS in the rotated basis can be expressed as

$$H_{TLS} = \frac{1}{2}ES_z, \quad (2.1)$$

where $S_z = \frac{1}{2}(\cos\theta\sigma_z + \sin\theta\sigma_x)$ with $\tan\theta = \Delta_0/\epsilon$. The σ_x and σ_z are Pauli's matrices. The energy difference between the two eigenstates $|\Psi_+\rangle$ and $|\Psi_-\rangle$ can be derived from the energy asymmetry parameter and the energy associated with the tunneling process

$$E = E_+ - E_- = \sqrt{\epsilon^2 + \Delta_0^2} \quad (2.2)$$

In the weak coupling regime, the coupling strength, g , is much smaller than the

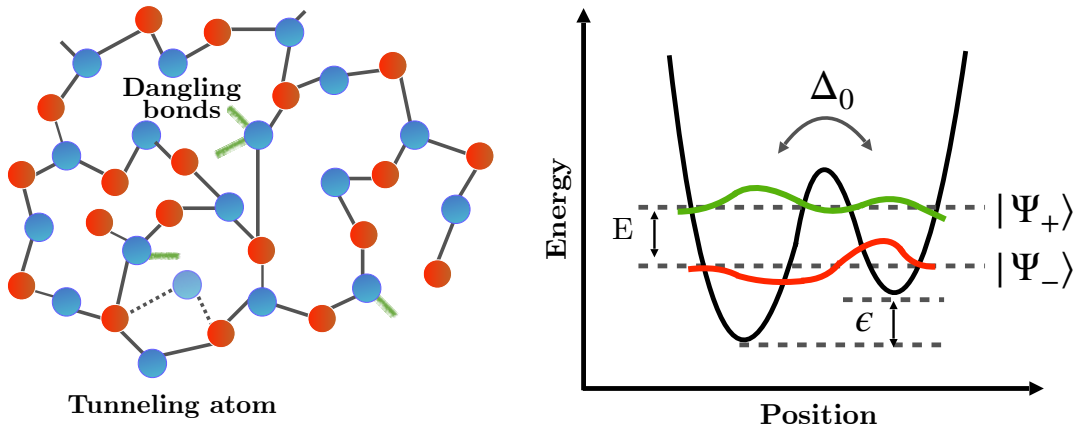


Figure 2.1: (Left) an illustration of the formation of TLS and (right) the double-well potential.

detuning between the TLS and the resonator, Δ_f , i.e. $g \ll \Delta_f$. The interaction between the TLS and the resonator is described by the dispersive Jaynes-Cummings Hamiltonian [17]

$$\hat{H}_{disp} = \frac{1}{2} \left(hf_0 - \frac{hg^2}{\Delta_f} \right) \hat{\sigma}_z + \left(hf_r - \frac{hg^2}{\Delta_f} \hat{\sigma}_z \right) \hat{a}^\dagger \hat{a}, \quad (2.3)$$

where f_0 represents the resonance frequency of the TLS, f_r is the frequency of the resonator. The detuning, Δ_f , is defined as the difference between the frequency of the TLS and the resonator, i.e. $\Delta_f = f_0 - f_r$. The operator \hat{a} and \hat{a}^\dagger are the resonator annihilation and the creation operator respectively. Equation 2.3 implies that the effective resonance frequency of the resonator depends on the state of the TLS. Consequently, its resonance frequency shifts. The shift of the resonance frequency is proportional to $\pm g^2/\Delta_f$, according to the TLS state.

Two-level systems can be categorized into two classes; coherent TLSs and incoherent TLSs. Coherent TLSs are characterized by a small decoherent rate $\Gamma_2 < E$, where E is typically larger than $k_B T$. They weakly interact with the environment and retain coherence on an experimental timescale. On the contrary, incoherent TLSs have $\Gamma_2 \geq E$. Having energy corresponding to a temperature of millikelvin, they can be thermally activated. The fluctuators strongly interact with their environment and incoherently switch their state on an experimental timescale. Hence, they are also referred to as thermal fluctuators [4, 18]. Since the resonator frequency $f_r \gg k_B T$, we can claim that the TLSs that contribute to the noise are the high-energy coherent TLSs, which have energy close to the resonator frequency. In the STM, coherent TLSs couple directly to a quantum device, leading to energy loss. Meanwhile, fluctuators interact weakly and can contribute to low-frequency noise only at low temperatures. Notably, in the STM, the interaction between coherent TLSs and incoherent TLSs is neglected.

However, recent studies have shown that, besides coupling to a quantum circuit, the coherent TLSs also interact with the surrounding fluctuators [5, 16, 19]. This coupling affects the energy splitting of the coherent TLSs. If the coherent TLS in-

interacts with only one thermal fluctuator, it can show a telegraphic energy drift. If the coherent TLS couples with many thermal fluctuators, there will be continuous time-dependent energy drift, known as spectral diffusion [20]. At the same time, the coherent TLS that undergoes spectral diffusion interacts with a resonator, leading to an energy shift of the resonator. The change of resonator energy corresponds to the fluctuation of the resonance frequency, which is translated to phase noise in a superconducting resonator [4]. This model is referred to as the generalized tunneling model (GTM) [5, 18], in which two modifications are made:

1. The interaction among TLSs cannot be omitted because it has a substantial impact on the TLS relaxation at low temperature.
2. The GTM considers a non-uniform probability density of the energy asymmetry ϵ .

One of the main predictions of the GTM is that the mutual interaction of the TLSs gives rise to the increased noise at low temperatures. Despite being counter-intuitive, it can be explained by the fact that coherent TLSs become more susceptible to interact with the thermal fluctuators when the temperature decreases. The detailed explanation and derivation are given in Ref.[18]. The frequency noise spectrum in the low-temperature limit ($T \ll hf_r/k_B$) depends on the temperature:

$$\begin{aligned} \frac{S_{\delta f}}{f_r^2} &\sim T^{(1-\mu)/2} && \text{in a strong electric field } \left(|\vec{\mathcal{E}}| \gg \mathcal{E}_c\right); \\ \frac{S_{\delta f}}{f_r^2} &\sim T^{-(1+\mu)} && \text{in a weak electric field } \left(|\vec{\mathcal{E}}| \ll \mathcal{E}_c\right). \end{aligned}$$

Here, the resonator frequency is denoted by f_r . The frequency noise spectrum is $S_{\delta f}$. T represents the temperature. The electric field and the critical electric field are expressed by \mathcal{E} and \mathcal{E}_c , respectively. The phenomenological parameter μ indicates the TLS density of states as $\rho(E) \propto E^\mu$. Previous experiments [5, 21, 22] have reported $\mu \approx 0.2 - 0.3$. In addition, the noise spectrum is power-dependent, i.e. $S_y \sim P^{-0.5}$ at the high field limit. While, in the low field limit, it is power independent.

The power spectral density of the frequency noise S_y can be estimated from the Fourier transform of the autocorrelation function [18],

$$S_y = \frac{S_{\delta f}}{f_r^2} = \lim_{T \rightarrow \infty} \int_0^T \int_0^T \frac{\langle \delta f(t_1) \delta f(t_2) \rangle}{f_r^2} e^{i\omega(t_1-t_2)} dt_1 dt_2. \quad (2.4)$$

Burnett *et al.* [23] have demonstrated that the noise power spectral density can be fitted with the general noise model.

$$S_y(f) = \frac{h_{-1}}{f^\nu} + h_0, \quad (2.5)$$

where h_0 is a white noise level, h_{-1} is a $1/f$ (flicker) noise level. The exponent ν indicates the strength of the low-frequency noise. If $\nu = 1$, the term h_{-1}/f portrays a true flicker noise process.

The resonance frequency fluctuation is translated to excessive phase noise in the resonator; whereas the amplitude noise is suppressed [4, 24]. Gao *et al.* [19, 25] have experimentally demonstrated the phase noise is caused by the TLSs and is equivalent to the fluctuation of the resonance frequency.

2.2 Surface acoustic wave resonator

A surface acoustic wave (SAW) resonator relies on the concept of piezoelectricity. The main elements of a SAW resonator are an interdigital transducer (IDT) and gratings. An IDT is a thin, patterned metal deposited on a piezoelectric material, depicted in Figure 2.2a. Once an oscillating voltage is applied to the two bus bars, the piezoelectric material below the IDT contracts and expands periodically, producing two SAWs in opposite directions. Each wave travels to the grating, reflects, and generates a standing wave in the cavity [26]. Figure 2.2b illustrates a one-port SAW resonator, which is used in this work.

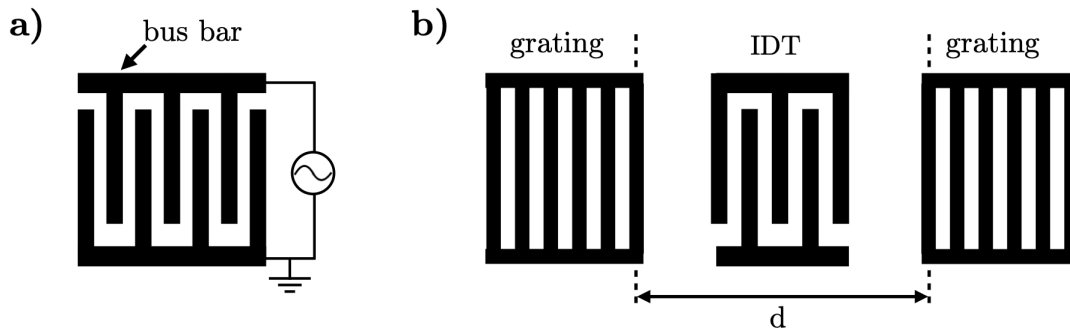


Figure 2.2: (a) an interdigital transducer (IDT) in operation and (b) a one-port SAW resonator.

To obtain a standing wave, the constructive interference condition must be satisfied:

$$d = \left(2n \pm \frac{1}{2}\right) \frac{\lambda}{2}, \quad (2.6)$$

where d is the distance between two gratings, λ is the wavelength of the SAW, and n is an integer. The velocity of SAW is approximately 3×10^3 m/s. Given that the frequency of SAW is in the GHz range, the wavelength of SAW is around one μm . The mode spacing of the SAW is thus very small, allowing an experiment at many different frequencies. Unlike a SAW, an electromagnetic (EM) wave travels with a velocity slightly lower 3×10^8 m/s in a microwave circuit. The wavelength of the EM wave is of the order of 10 cm, which is larger than the resonator length. As the mode spacing of the EM wave is large, an experiment with a microwave resonator is limited to one or a few frequencies. Typically, a resonator is characterized by its resonance frequency f_r and a quality factor Q , which is defined as a ratio of energy stored in a resonator and energy loss per radian. The internal loss is described by an internal quality factor Q_i . The external loss, caused by coupling with other parts of a circuit, is described by a coupling or external quality factor Q_C . The total or loaded quality factor, Q_L , is determined by

$$\frac{1}{Q_L} = \frac{1}{Q_i} + \frac{1}{Q_C}. \quad (2.7)$$

There are three possible coupling regimes, characterized by the coupling coefficient k , where $k = Q_i/Q_C$:

$$\begin{aligned}
Q_i > Q_C \quad (k > 1) & \quad \text{overcoupled,} \\
Q_i = Q_C \quad (k = 1) & \quad \text{critically coupled,} \\
Q_i < Q_C \quad (k < 1) & \quad \text{undercoupled.}
\end{aligned}$$

Given the characteristics of a resonator, one can estimate the resonator response. In this study, we measure the signal reflected from a resonator in terms of the reflection coefficient S_{11} . The mathematical expression of S_{11} for an ideal resonator with respect to Q is written as

$$S_{11}(f) = 1 - \frac{2(Q_L/Q_C)}{1 + 2iQ_L(\frac{f-f_r}{f_r})}, \quad (2.8)$$

where f , and f_r represent the probing frequency, and the resonance frequency, respectively. Amplitude and phase response as functions of the probing frequency are demonstrated in Figure 2.3. If a resonator is overcoupled with a feedline, dissipation is low. Therefore, most of the phonons can leave the resonator and travel back to be measured. When the resonator is critically coupled, phonons are maximally transferred between the feedline and the resonator. Thus, the reflection coefficient is suppressed to zero at the resonance frequency. In the undercoupled case, phonons are dissipated in the resonator.

2.3 Lock-in amplifier

A lock-in amplifier is used for measuring a weak signal at one specific frequency by comparing the input with a reference signal. Suppose an input signal is described by

$$V_{in} = A_{in} \sin(\omega_{in}t + \phi_{in}), \quad (2.9)$$

and a reference signal is represented by

$$V_{ref} = A_{ref} \sin(\omega_{ref}t + \phi_{ref}). \quad (2.10)$$

where the frequency of the input ω_{in} and the reference frequency ω_{ref} are equal. The product of the two signals has one DC and one AC component. The AC component will be removed by a low-pass filter; whereas a DC component remains. The output signal is

$$V_{out} = \frac{A_{in}A_{ref}}{2} \cos(\phi_{in} - \phi_{ref}). \quad (2.11)$$

Since the amplitude and phase of the reference signal are known, the amplitude of the input signal can be determined [27].

2.4 Frequency mixer

A frequency mixer is an electrical circuit for generating a signal with the desired frequency from two other input signals. A general mixer has three ports, namely local oscillator (LO), radiofrequency (RF) and intermediate frequency (IF). Depending on the choices of input ports, one can choose to perform either up-conversion or

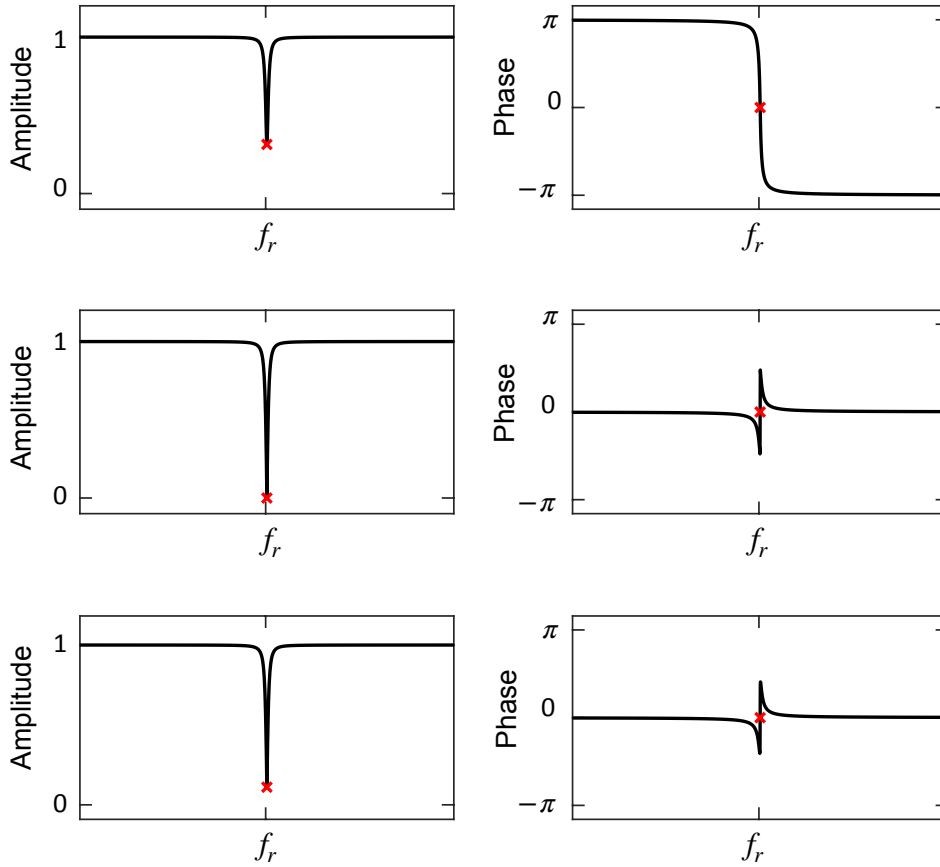


Figure 2.3: Amplitude and phase response of a SAW resonator as a function of frequency in three different coupling regimes: (top) overcoupled, (middle) critically coupled, and (bottom) undercoupled. The red crosses represent amplitude and phase response at the resonance frequency.

down-conversion.

To shift a signal from one frequency range to a higher range, one performs up-conversion by taking the LO and the IF port as inputs. The output from the RF port will have the frequency

$$f_{RF} = f_{LO} \pm f_{IF}. \quad (2.12)$$

On the other hand, in down-conversion, the LO and the RF are inputs. The down-converted signal comes out from the IF port with frequency

$$f_{IF} = f_{LO} \pm f_{RF}. \quad (2.13)$$

The output from both cases has two symmetric sidebands located on each side of the LO in the frequency domain. Nonetheless, in this work, only high sideband is desired. The lower sideband could cause interference when measuring the resonator. Therefore, instead of a normal mixer, an I/Q mixer is employed to suppress the lower sideband. An I/Q mixer works in the same principle as a normal mixer. The difference is that it has 4 ports as the IF is separated into two ports, i.e. I and Q. I

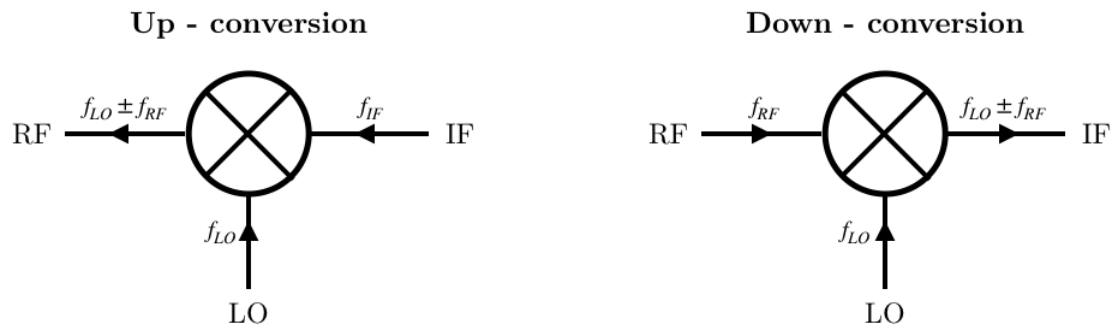


Figure 2.4: Frequency mixer basic operation

stands for in-phase and Q stands for quadrature. When the I and the Q ports have $\frac{\pi}{2}$ phase shift, the lower sideband will be suppressed, resulting in a center frequency and only high sideband. The derivation of up-conversion and down-conversion equations for an I/Q mixer is provided in Ref. [28].

3

Methods

To observe correlations of resonance frequency fluctuations of different modes, we investigate the reflection coefficient S_{11} while driving many resonance modes of a SAW resonator simultaneously. The experiment requires a signal generator that can produce and measure multiple tones simultaneously. We utilize the multi-frequency lock-in amplifier (MLA), which operates in the MHz range, to drive and read many frequencies at the same time. Since resonance frequencies of the SAW resonator are in the GHz range, the MLA signal has to be up-converted before sending it to the sample and down-converted before reading. This process is performed by a frequency mixer. Section 3.1 gives details of the devices used in this study and demonstrates the experimental setup. Measurement methods are explained in section 3.2, 3.3, and 3.4. The S_{11} data obtained from the measurement are converted to the resonance frequency, discussed in section 3.5. Finally, the resonance frequency fluctuations from different modes are investigated by considering Welch power spectral density, Allan deviation, correlation coefficient, and magnitude-squared coherence as described in section 3.6.

3.1 Experimental setup

3.1.1 SAW resonator

The SAW resonator used in this work is made of aluminum on a GaAs substrate. The device is composed of two Bragg mirrors, separated from each other by 1440 μm . Each mirror has 800 fingers. An IDT is located at the center of the cavity, functioning as an input and an output port. More details about the SAW resonator are described in Ref. [10]. The device has 20 resonance modes, ranging from 2.37 to 2.41 GHz. Each mode is located approximately 2 MHz apart. However, the free spectral range between neighboring mode is not exactly equal. Figure 3.1 shows the SAW resonator and its spectrum. The device is mounted in a dilution refrigerator and cooled down to cryogenic temperature, around 10 mK.

3.1.2 Multi-frequency lock-in amplifier

The multi-frequency lock-in amplifier (MLA) has the same working principle as the lock-in amplifier explained in Chapter 2, although the implementation is more complicated. MLA S/N3104 [29] can produce and measure up to 32 tones simultaneously. It operates from 0 to 80 MHz, and the input and output ports have 50 Ω

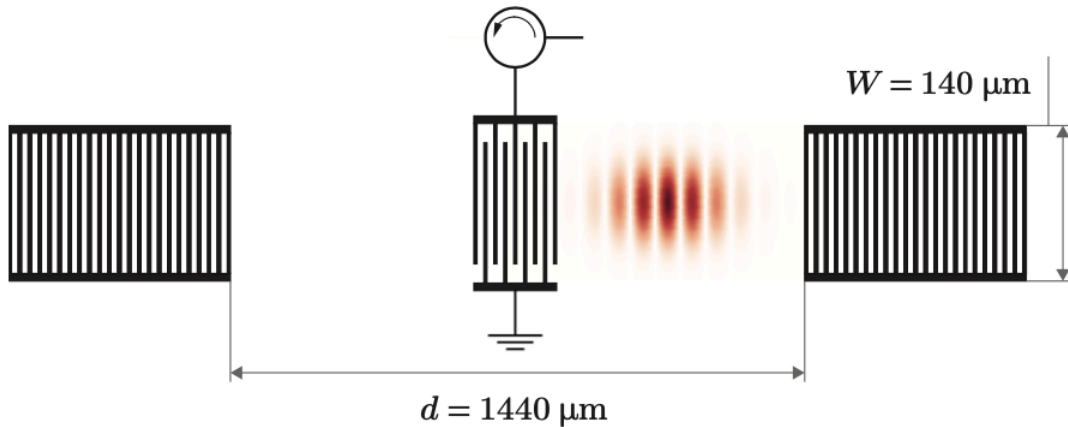


Figure 3.1: The SAW resonator used in this study [10].

impedance. The software is programmed in python. More details about set-up and scripts are given in Appendix A.

3.1.3 Frequency conversion

Frequency conversion is performed by an up-conversion and a down-conversion mixer in a frequency modulation board [28]. Both frequency mixers are I/Q mixers, to suppress the lower sideband resulting from frequency mixing. To drive only a high sideband, it requires two input signals from the I and the Q port with the same amplitudes ($A_I = A_Q$), but phase of the signal in the I port must be $\frac{\pi}{2}$ ahead of that in the Q port ($\phi_I - \phi_Q = \frac{\pi}{2}$).

3.1.4 Measurement configuration

Figure 3.3 displays an overview of the measurement setup. The LO is set to 2.32 GHz. The MLA generates a multifrequency signal to the input I and Q ports of the mixer. The up-converted signal is sent through the RF output port to the SAW resonator, which is installed in a dilution refrigerator as shown in Figure 3.2. The signal reflected from the resonator is amplified by a low-temperature amplifier in the cryostat, sent to the input RF port of the conversion board, and down-converted to MHz frequencies, which will be read by the MLA. To enhance the signal-to-noise ratio, a room temperature amplifier is used to boost the signal from the resonator before the down-conversion. A 20 dB attenuator is also added to the MLA output port, enabling measurements at low power. Additionally, a bandpass filter 2375-2425 MHz is installed at the output port of the mixer board to suppress unwanted sidebands.

3.2 SAW resonator characterization

To characterize the SAW resonator, we sweep the frequency from 2.37 to 2.40 GHz and measure amplitude and phase response at input power -47, -57, and -67 dBm.

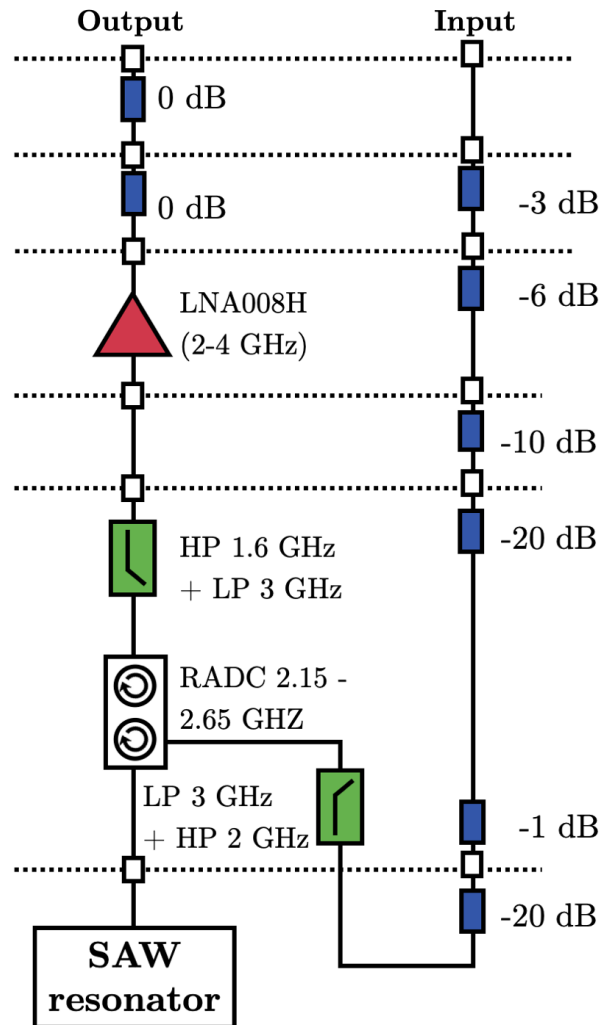


Figure 3.2: A diagram illustrating the SAW resonator installed in a dilution refrigerator.

These estimated powers are calibrated with a spectrum analyzer. The frequency resolution is 1 kHz, allowing to obtain a good parameter fitting result later on. Since the internal quality factor of a resonator is power-dependent [30], we measure the amplitude and phase response of each SAW mode when it is driven by a similar input power to that in the phase noise measurement. The SAW mode characterization is carried out by pumping all resonance modes simultaneously while performing the frequency sweep. The input amplitude of the sweeping tone is set to be 10 dBm lower than the amplitudes of the lock-in tones.

Subsequently, the data are divided into modes and fitted for Q values using the CircleFit notebook [31]. Figure 3.4 shows the resonator response at input power -47 dBm. There are 14 resonance modes within the range of 2.37 - 2.40 GHz. A python script for frequency sweeping is included in Appendix B.

Based on these frequency sweep data, we can extract resonance frequencies of the SAW resonator and define our probing frequencies for measuring the phase noise.

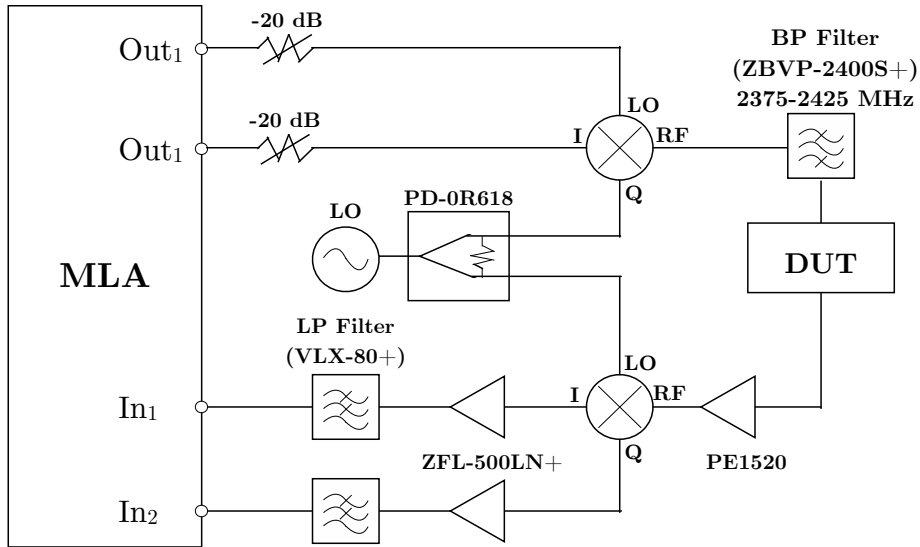


Figure 3.3: A circuit diagram representing the experiment setup. The LO pumps a GHz signal. The MLA generates a multifrequency signal to be up-converted by the up-conversion mixer. The signal is up-converted to the GHz range. The up-converted signal is sent to the SAW device. The reflected signal goes to the bandpass filter and the room temperature amplifier before being down-converted by the down-conversion mixer. Finally, the down-converted signal is read by the MLA.

The position that gives the highest sensitivity for observing resonance frequency fluctuations is, ideally, at $f = f_r$, which corresponds to the minimum point in amplitude and the steepest point of slope in the phase curve. To ensure that the probing frequency is at the optimum point, we apply the Nelder-Mead minimization method [32] to obtain the frequency that gives the minimum amplitude for each resonance mode.

3.3 Normalizing the number of phonons in the resonator

Due to the different quality factors among the different resonance modes, driving all resonance modes using the same input power causes an unequal number of phonons. For better comparison, we pump each resonance mode using different power in order to obtain the same phonon number in each mode. According to Kirch *et al.* [33], the number of photons in a microwave resonator in a steady-state, $\langle N \rangle$, is estimated by

$$\langle N \rangle = 4 \frac{Q_L Q_L}{\omega_r Q_C} \frac{1}{1 + (2Q_L \Delta / \omega_r)^2} \frac{P}{\hbar \omega_p}, \quad (3.1)$$

where ω_r is the resonance frequency, ω_p is the pumping frequency, and the detuning Δ is defined as $\omega_p - \omega_r$. P is the input power, defined as $\hbar \omega \times$ rate of phonons arriving in the resonator [34]. The quality factors Q_L and Q_C are derived by fitting the frequency sweep data. In this case, we pump the resonator at its resonance

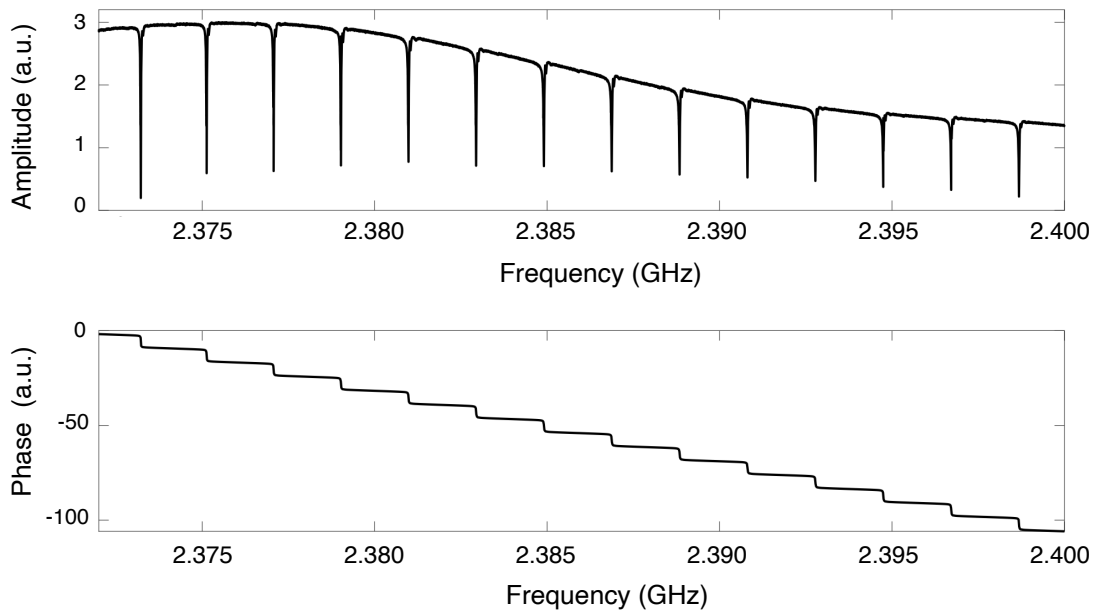


Figure 3.4: Amplitude and phase response of the SAW resonator, measured in reflection at input power -47 dBm.

frequency ($\omega_p = \omega_r$). Hence, the detuning $\Delta = 0$. Therefore, by using the amplitude response, A_{ref} , from one particular mode as a reference, the output amplitude of mode i^{th} , A_i , from the MLA is scaled by

$$A_i = \frac{Q_{L,ref}}{Q_{L,i}} \frac{\omega_{0,i}}{\omega_{0,ref}} \sqrt{\frac{Q_{C,i}}{Q_{C,ref}}} A_{ref}. \quad (3.2)$$

3.4 Phase noise measurement

After defining the probing frequencies, we use the MLA to drive the SAW resonator and measure phase noise as a function of time. When performing a phase noise measurement, we add an off-resonance tone at 2.39 GHz in addition to the resonance frequencies of the SAW resonator. The objective of this off-resonance tone is to be used as a control tone, which will indicate whether the measured signal is caused by the SAW device or by other perturbations from the environment. As the reflection coefficient S_{11} is a complex number, the measured data is recorded in the form of amplitude and phase. The sampling rate of the measurement is 100 Hz. We take an average of the measured data every 10 points to increase the signal-to-noise ratio. Hence, the sampling rate of the data is 10 Hz. According to Burnett *et al.* [35], the TLS switching rate is 75 μ Hz - 2 mHz. Hence, we perform each measurement for 2.6×10^4 seconds (approximately seven hours) in order to capture the TLS switching.

3.5 Resonance frequency calculation

We calculate the frequency from the measured reflection coefficient S_{11} using the parameters obtained by fitting the resonance profile. According to Probst *et al.* [31], the reflection coefficient of a superconducting resonator is described by

$$S_{11} = -ae^{-i(\pi-\alpha)} \left[1 - \frac{2(Q_L/Q_C)e^{i\phi_0}}{1 + 2iQ_L\left(\frac{f-f_r}{f_r}\right)} \right], \quad (3.3)$$

where a is an amplitude scaling coefficient. A phase shift is denoted by α . The loaded quality factor and the external quality factor are represented by Q_L and Q_C , respectively. An impedance mismatch is accounted for by the parameter ϕ_0 . The term $-ae^{-i(\pi-\alpha)}$ represents effects from the environment, i.e. effects not being contributed by the SAW resonator. In addition, there is a frequency-dependent phase shift created by a finite speed of light and the cable length, referred to as an electrical delay or a cable delay τ_0 . Taking these effects and the background into account, the reflection coefficient S_{11} that is measured from the experiment can be expressed as

$$S_{11} = 10^{m(f-f_{rotate})} \times e^{-2\pi i f \tau_0} \times \left[-ae^{-i(\pi-\alpha)} \left(1 - \frac{2(Q_L/Q_C)e^{i\phi_0}}{1 + 2iQ_L\left(\frac{f-f_r}{f_r}\right)} \right) \right], \quad (3.4)$$

where f_{rotate} and the parameter m are obtained from the CircleFit. Considering equation 3.4, there is only one unknown, i.e. resonance frequency f_r . Hence, it can be determined by simply solving this equation. Firstly, the equation is re-written as

$$S_{11} = A_m e^{\phi_m} = A_{env} e^{i\phi_{env}} \left(1 - \frac{2(Q_L/Q_C)e^{i\phi_0}}{1 + 2iQ_L\left(\frac{f-f_r}{f_r}\right)} \right), \quad (3.5)$$

where A_m , ϕ_m , A_{env} , and ϕ_{env} are measured amplitude, measured phase, amplitude, and phase shift of signal contributed by the environment, respectively. The equation can be re-arranged to

$$e^{-i\phi_0} - \frac{A_m}{A_{env}} e^{i(\phi_m - \phi_{env} - \phi_0)} = \frac{2(Q_L/Q_C)}{1 + 2iQ_L\left(\frac{f-f_r}{f_r}\right)}. \quad (3.6)$$

Multiplying both sides of equation by $e^{i\pi/2}$ yields

$$e^{-i(\phi_0 - \pi/2)} - \frac{A_m}{A_{env}} e^{i(\phi_m - \phi_{env} - \phi_0 + \frac{\pi}{2})} = \frac{2i(Q_L/Q_C)}{1 + 2iQ_L\left(\frac{f-f_r}{f_r}\right)}. \quad (3.7)$$

Let us call the term of the left a complex number Z , where

$$Z = \frac{4(Q_L/Q_C)Q_L\left(\frac{f-f_r}{f_r}\right) + 2i(Q_L/Q_C)}{1 + 4Q_L^2\left(\frac{f-f_r}{f_r}\right)^2}. \quad (3.8)$$

The phase, δ , of the complex number is determined by

$$\delta = \begin{cases} -\frac{\pi}{2} - \arctan\left(2Q_L\left(\frac{f-f_r}{f_r}\right)\right) & \text{for } y < 0, \\ \frac{\pi}{2} - \arctan\left(2Q_L\left(\frac{f-f_r}{f_r}\right)\right) & \text{for } y > 0. \end{cases} \quad (3.9)$$

Finally, the resonance frequency can be obtained.

$$\frac{f - f_r}{f_r} - 1 = \begin{cases} -\frac{1}{2Q_L} \tan\left(\frac{\pi}{2} + \delta\right) & \text{for } y < 0, \\ \frac{1}{2Q_L} \tan\left(\frac{\pi}{2} - \delta\right) & \text{for } y > 0. \end{cases} \quad (3.10)$$

Then, the frequency fluctuation Δf_r is determined by subtracting the calculated frequency with its corresponding resonance frequency. Subsequently, the correlation between fluctuations of each mode is computed. This resonance frequency calculation is performed in MATLAB.

3.6 Data analysis

Resonance frequencies determined from the measured reflection coefficient S_{11} is investigated to see the correlation between different modes. We estimate the power spectral density and Allan deviation to identify types of noise. Moreover, relationships across different modes are evaluated by examining the correlation coefficient of Δf_r , and magnitude-squared coherence.

3.6.1 Welch power spectral density

The power spectral density of the resonance frequency fluctuation is estimated using Welch's method. Unlike a standard spectrum estimation approach, Welch's method divides the signal into overlapping segments and applies a window function before performing a discrete Fourier transform. Here, the data are divided into eight segments with 50% overlap. The squared magnitude of the result is the Welch power spectral density. This technique gives a lower frequency resolution in return for reduced noise. The resulting power spectral density is subsequently compared with a general noise model

$$S_y(f) = \frac{h_{-1}}{f^\nu} + h_0 \quad (3.11)$$

where h_{-1} is a flicker noise level. ν is an exponent associating with the strength of the low-frequency noise. h_0 is a white frequency noise level.

3.6.2 Allan deviation

The Allan deviation (ADEV) is the square root of the Allan variance (AVAR), which is introduced to describe the stability of signal caused by noise processes, such as frequency drift. This time-analysis method is useful for investigating long-timescale processes, which are more difficult to analyze from the power spectral density. The mathematical expression of the AVAR can be written as

$$\sigma_y^2(\tau) = \frac{1}{2} \langle (\bar{y}_{n+1} - \bar{y}_n)^2 \rangle = \frac{1}{2\tau^2} \langle (x_{n+2} - 2x_{n+1} + x_n)^2 \rangle \quad (3.12)$$

where τ is an observation period, \bar{y}_n is the n^{th} fractional frequency averaged over the period τ . The n^{th} time error function x_n is derived from the difference between the expected nominal time and the actual normal time. The mathematical expression

of the averaged fractional frequency over an observation time τ is

$$\bar{y}(t, \tau) = \frac{1}{\tau} \int_0^\tau y(t + t_\nu) dt_\nu = \frac{x(t + \tau) - x(t)}{\tau}. \quad (3.13)$$

Straightforwardly, the ADEV is the square root of the AVAR,

$$\sigma_y(\tau) = \sqrt{\sigma_y^2(\tau)}. \quad (3.14)$$

The ADEV is used as a tool for addressing the source of fluctuation in qubits [35]. According to the power noise law, a $1/f$ noise process shows a constant ADEV; while a white noise exhibits $1/\sqrt{\tau}$ dependent behavior [36]. The benefit of using the ADEV is that it can reveal the TLS-based Lorentzian noise because the Lorentzian noise produces a peak, whereas there is no power-law noise process that can produce local maxima in the ADEV.

3.6.3 Correlation coefficient

The Pearson correlation coefficient describes the strength of the linear relationship between the relative change of two variables x and y , which is calculated by

$$\rho(x, y) = \frac{1}{N-1} \sum_{i=1}^N \left(\frac{x_i - \mu_x}{\sigma_x} \right) \left(\frac{y_i - \mu_y}{\sigma_y} \right), \quad (3.15)$$

where μ and σ are the mean and standard deviation, respectively. The correlation coefficient value is between -1 (total negative linear correlation) and 1 (total positive linear correlation).

3.6.4 Magnitude-squared coherence

Coherence, in signal processing, describes the linear correlation of two zero-mean variables at each frequency [37]. The coherence function, c_{xy} , of the variable x and y is defined as

$$c_{xy}(f) = \frac{P_{xy}(f)}{[P_{xx}(f)P_{yy}(f)]^{1/2}}, \quad (3.16)$$

where $P_{xx}(f)$ and $P_{yy}(f)$ are the power spectral densities of x and y , respectively. $P_{xy}(f)$ is the cross power spectral density of x and y . These power spectral densities are computed using Welch's method. Note that the coherence c_{xy} is a complex number. The magnitude of the coherence function ranges from 0 to 1. If $|c_{xy}| = 1$, the variable x and y are completely coherent. If $|c_{xy}| = 0$, then the two variables are totally uncorrelated. Equation 3.16 has a geometrical interpretation as the magnitude of the cosine of the angle between the vector $\{x(t)\}_{-\infty}^{\infty}$ and $\{y(t)\}_{-\infty}^{\infty}$ [38].

In this work, we calculate the magnitude-squared coherence, C_{xy} , which is defined as

$$C_{xy}(f) = |c_{xy}(f)|^2 = \frac{|P_{xy}(f)|^2}{P_{xx}(f)P_{yy}(f)}. \quad (3.17)$$

The magnitude-squared coherence, C_{xy} , is a real number, in which the interpretation is more straightforward than the coherence function c_{xy} . If the variable x and y are ergodic and the system function is linear, the C_{xy} indicates how well the variable y can be estimated from the variable x using the linear least-square function.

4

Results and discussion

This chapter presents the characteristics of the SAW resonator at various input powers and temperatures. Following the resonator profiles in section 4.1, the phase noise measurement results and the correlations of the resonance frequency fluctuations between different modes are discussed in section 4.2. The noise process identification is explained in subsection 4.2.1. The following subsection 4.2.2 discusses the correlation of the frequency noise. Subsection 4.2.3 describes the power dependence of resonance frequency fluctuations at a fixed temperature, approximately 10 mK. Subsection 4.2.4 discusses the temperature dependence of the resonance frequency fluctuations at input power -47 dBm. Finally, the investigation of local TLS effects is explained in section 4.3.

4.1 SAW resonator profile

The SAW resonator characteristics are derived by performing a frequency sweep and measuring the amplitude and the phase responses at different input powers; -47, -57, and -67 dBm. The results are displayed in Figure 4.1. Subsequently, the data from each mode are fitted using the CircleFit notebook [31].

The quality factors extracted from the fitting are presented in Figure 4.2. When driving with a high input power, more TLSs are saturated, resulting in less energy loss in the resonator. Hence, the internal quality factor of the resonator is high. Applying input power -47 dBm, the internal quality factors are larger than the external quality factors. All resonance modes are then overcoupled. At the low power, -67 dBm, the extracted internal quality factors are smaller than the coupling quality factors. The resonator becomes undercoupled. Applying -57 dBm input drive, the edge modes, for example, mode #1, #2, #13, and #14, are undercoupled.

4.2 Investigating the noise caused by TLSs

The time traces of the reflection coefficients are recorded in terms of amplitude and phase. An example of the time traces is shown in Figure 4.3 - 4.4. Note that each trace in all plots is normalized by its standard deviation and shifted vertically for better visualization. The amplitude and phase plots also show the responses from the control tone, which is an off-resonance tone located at 2.39 GHz. The control traces remain steady for the entire measurement timescale, confirming that there is no external perturbation from the environment.

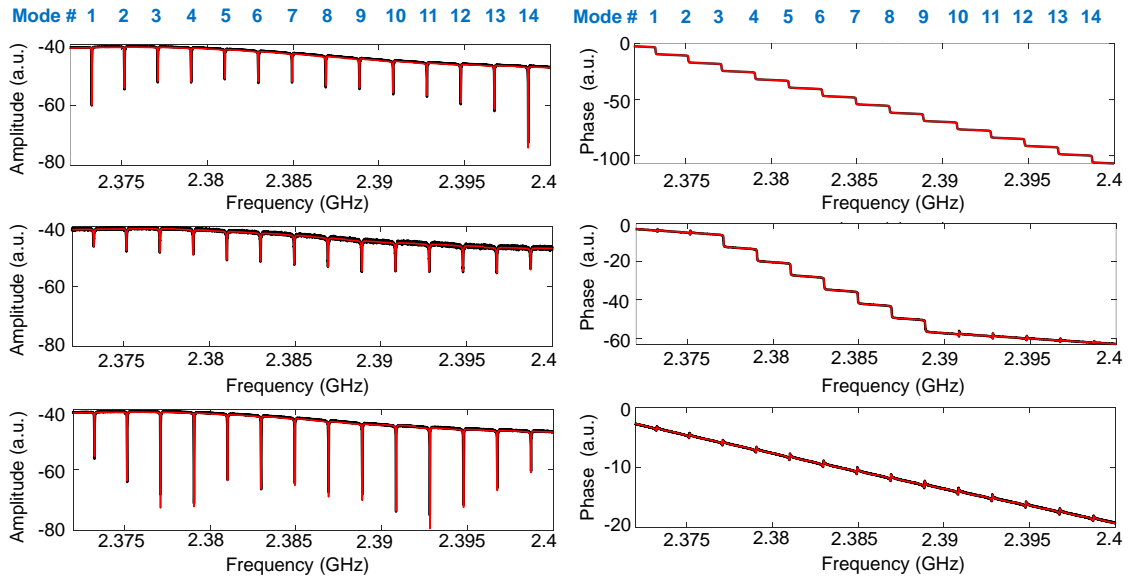


Figure 4.1: Amplitude and phase responses of a the SAW resonator response at input power (top) -47 dBm, (middle) -57 dBm, and (bottom) -67 dBm. The blue text indicates the mode index, which will be referred to in the following discussions.

Considering the phase traces, there are noticeable similar features in many modes, indicating the significant correlation between different modes. For example, there are spikes in the phase traces at time 1×10^4 seconds. These characteristics are preserved in the resonance frequency shifts. In the Δf_r plot, the first seven modes exhibit negative fluctuations. Notably, the magnitude of the fluctuations decreases as the mode number increases. For 9th and 10th modes, the peaks diminish, hence, the correlations. Interestingly, the resonance frequency shifts become positive in the last four modes, implying the reverse correlations with the data from the first mode. To determine the correlations of the frequency noise induced by the interaction of TLSs, we first identify the noise processes. Then, the relationships of the noise between different modes are analyzed in both the time and frequency domain by calculating the correlation coefficient and the magnitude-squared coherence, respectively. The results are discussed in the following subsections.

4.2.1 Noise process identification

As mentioned in Chapter 2, the frequency noise induced by the TLSs is expected to show $1/f$ characteristics. However, there can be other noises, such as the noise exhibiting the Lorentzian processes [35] and the noise from instruments [39], added to the data. The sources of the noises are identified by examining the power spectral density of the frequency shifts and the Allan deviation of the resonance frequency. In addition, we carry out a long measurement (24 hours), using -47 dBm input power. The results and analysis of the measurement are included in Appendix C.1.

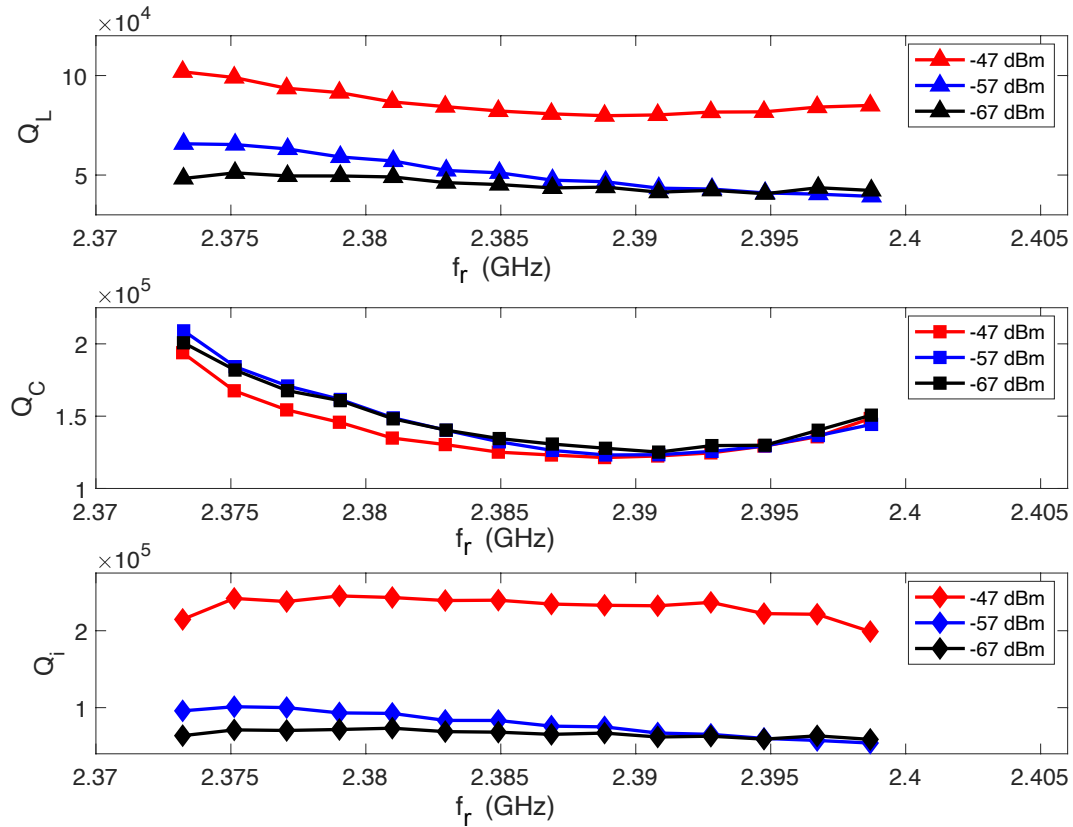


Figure 4.2: (Top) the loaded quality factors Q_L , (middle) the external quality factors Q_C , and (bottom) the internal quality factors Q_i of the SAW resonator at each frequency when using different input powers.

4.2.1.1 Noise power spectral density

The power spectral density (PSD) of the resonance frequency shift Δf_r is shown in Figure 4.5. The recorded trace has 2.6×10^5 data points. Welch's method divides the data trace into eight segments with 50% overlap. Thus, there are approximately 2.9×10^4 points per segment. Given that the sampling rate of the data, f_s , is 10 Hz, the frequency resolution is $f_s/\text{number of points} \approx 3 \times 10^{-4}$ Hz, which defines the lowest frequency that can be observed. The highest frequency component observable in the PSD is limited by the Nyquist frequency $f_N = f_s/2 = 5$ Hz.

Fitting the PSD to the $1/f$ model, h_{-1}/f^ν , gives $\nu = 0.74$, $h_{-1} = 1.49 \times 10^{-16}$. The poorly fitted blue curve with the data is evidence that it is not a pure $1/f$ noise characteristics. Instead, adding the Lorentzian noise spectrum, i.e. $A\gamma/(f^2 + \gamma^2)$, gives a better result, shown as the black line in Figure 4.5. Fitting the PSD with the function $A\gamma/(f^2 + \gamma^2) + h_{-1}/f$ yields $A = 4.28 \times 10^{-16}$, $\gamma = 0.14$, and $h_{-1} = 1.92 \times 10^{-17}$.

4.2.1.2 Allan deviation

In addition to the PSD, we calculate the Allan deviation (ADEV). The ADEV also confirms that there is a Lorentzian noise process dominated in the time scale from

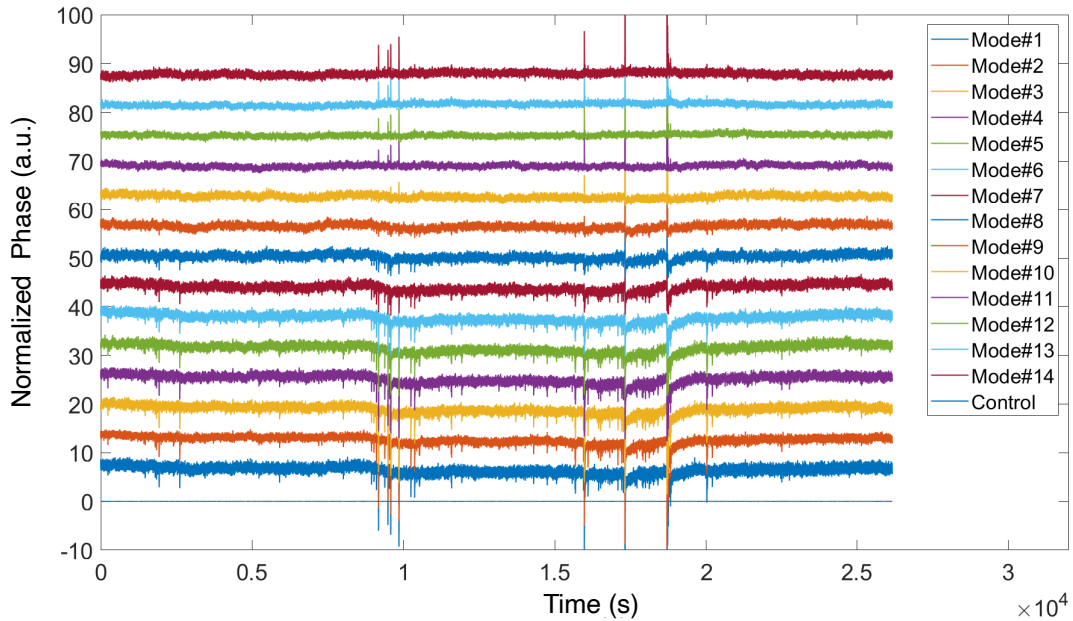


Figure 4.3: The time traces of the measured phases. The bottom trace represents the control tone measured at 2.39 GHz, which is off-resonance with the SAW modes.

1 - 10 seconds, shown as the local maximum in Figure 4.6. This Lorentzian noise has been observed in the previous experiments reported by Burnett *et al.* [35] and Müller *et al.* [40]. This effect is attributed to a single dominant low-frequency TLS.

4.2.2 Correlations of the resonance frequency fluctuations

4.2.2.1 Correlation coefficients

The correlation coefficients between any two time traces are calculated and displayed in the matrices as illustrated in Figure 4.7. The matrix element a_{ij} represents the correlation between the trace i^{th} and j^{th} .

The frequency shift of each mode of the SAW resonator shows correlation as they are caused by the coupling with the same ensemble of surrounding TLSs. The variation of the correlation coefficients between each pair of modes can be explained by the Jaynes-Cummings hamiltonian shown in Equation 2.3. As the interaction between TLSs and the resonator depends on the inverse of the detuning Δ_f , the TLSs located further away in frequency interact more weakly. Hence, the magnitude of the correlations reduces as the detuning Δ_f between the modes increases. Notably, at a particular distance, the correlation diminishes and becomes negative as the pair is located further apart. The negative correlations cannot be described using Equation 2.3. However, the derived correlation coefficients are reasonable as we can observe some events occurring in the opposite direction shown in the time trace plots in Figure 4.3 - 4.4. Therefore, a further theoretical consideration is required to explain this experimental result.

Figure 4.8 plots the correlation coefficients as a function of detuning. Note that the graph is symmetric and contains redundant data points as the correlation coefficient

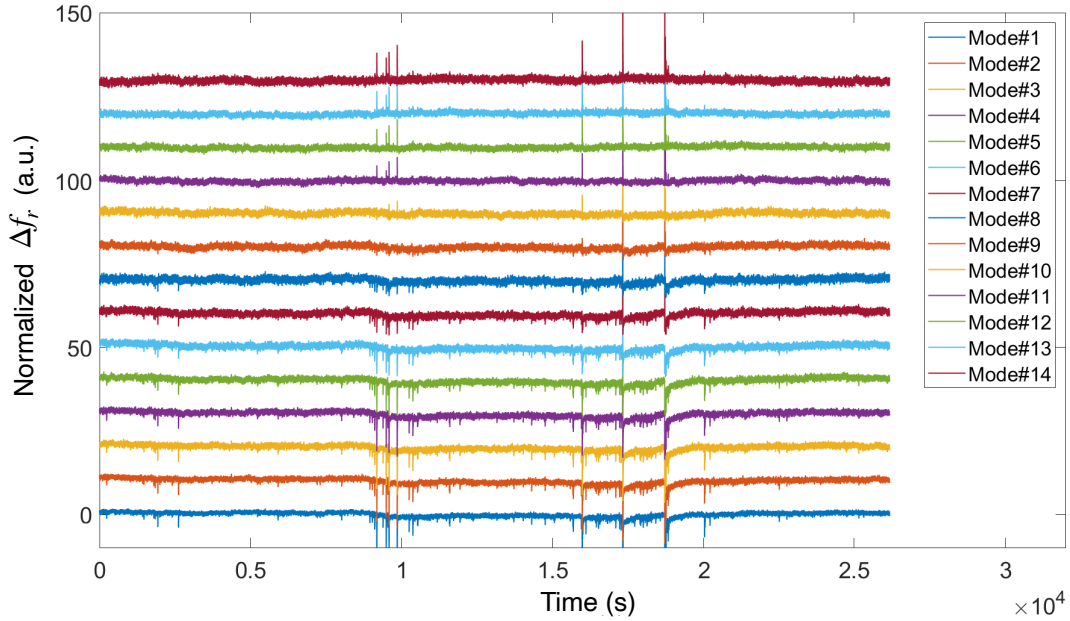


Figure 4.4: The time trace of the calculated resonance frequency shifts calculated using Equation 3.10. The time trace of the calculated resonance frequency shifts. Note that there is no converted frequency from the control tone because it does not correspond to any resonance mode.

of mode i^{th} and j^{th} is identical to the correlation of mode j^{th} and i^{th} .

4.2.2.2 Magnitude-squared coherence

The magnitude-squared coherence, C_{xy} , plots suggest that the frequency noises are correlated at low frequencies, up to 1 Hz. Figure 4.9 shows an example of the magnitude-squared coherence of mode #1 vs mode #2, #11, and #14. In the top panel, the values between mode #1 and #2 are close to 1 from 10^{-4} to 0.5 Hz. After that, they drop significantly. Considering the magnitude-squared coherence between mode #1 with mode #11, the coherence substantially decreases. This is clearly seen for frequencies lower than 10^{-3} Hz. These results conform to the correlation matrix in Figure 4.7 that the correlation decreases with increasing detuning. For the last mode in the bottom panel, the coherence increases again, indicating that there is a high similarity between mode #1 and #14. This result also agrees with the previous analysis but we know that it is an anti-correlation as shown by the correlation matrix. Another key observation is that there is also relatively high coherence in the frequency of 0.1 - 1 Hz, which is the range that Lorentzian noise dominates.

4.2.3 Power dependence of the resonance frequency shifts

The noise caused by TLSs has been found to exhibit $1/P^{0.5}$ dependence [19, 25, 41, 42]. The frequency noise PSD derived from varying input power, P , is illustrated

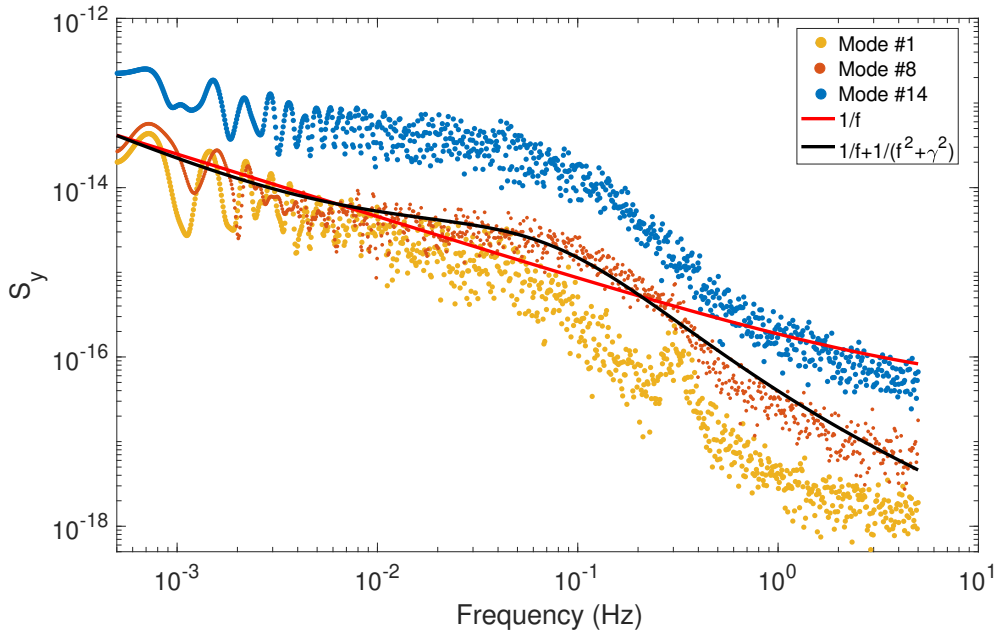


Figure 4.5: Welch power spectral density (S_y) of the resonance frequency fluctuation Δf_r . Note that only mode #1, #8 and #14 are displayed. The fitted functions are fitted to mode #8.

in Figure 4.10. The plot shows that the noise level decreases as the applied power increases, except when using input power -47 dBm. At this power, the PSD of the frequency noise is remarkably high in the frequency range of $10^{-4} - 1$ Hz, which corresponds to the range that the Lorentzian noise process dominates. Since the input power has an impact on the quality factor of the resonator, we take this factor into account when analyzing the noise level. Therefore, we investigate the relationship between the noise level and the normalized number of phonons, instead of considering only the pumping power. The frequency noise, $S_y(0.1 \text{ Hz})$, cannot be fitted to the theoretical prediction that $S_y \sim 1/P^{0.5}$ because of the high noise levels at $\langle N \rangle \sim 10^3$, which corresponds to -47 dBm input power. The results infer that the single dominant TLS, observed at -47 dBm input drive, causes more pronounced frequency noise and affects the noise at all modes.

Although Burnett *et al.*[21] and Müller *et al.*[40] have reported the presence of Lorentzian noise process caused by a single dominant TLS, the relationship for the power dependence of the data has not been demonstrated. The source of the variation of the exponent, therefore, remains unknown. Hence, more measurements and analysis are required to identify the power dependence of frequency noise in the SAW resonator.

Considering the frequency noise correlations between different modes derived from the measurement at 10 mK, the correlation coefficients vary the most when using -47 dBm input drive, which corresponds to approximately $\langle N \rangle \sim 10^3$. Figure 4.11 is an example of the power-dependent correlations obtained from mode #1, #5, #10, and #14.

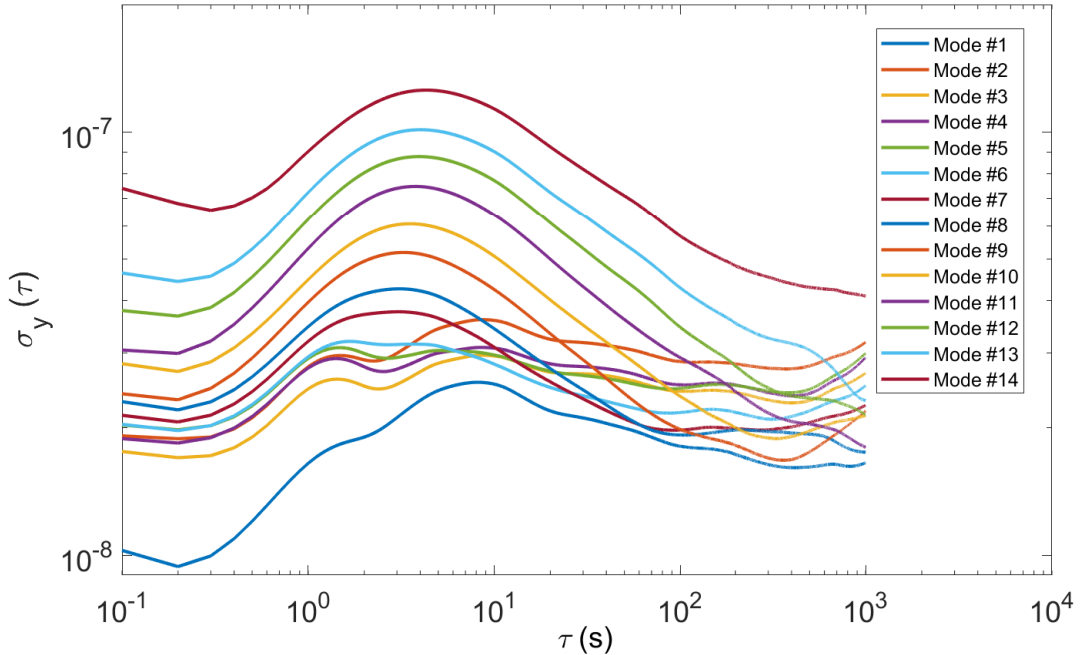


Figure 4.6: Allan deviation of the resonance frequency f_r . The peaks indicate the presence of a single dominant TLS, which dominates in time period of 1 - 10 s.

4.2.4 Temperature dependence of the resonance frequency shifts

As mentioned in Chapter 2.1, the TLS-induced noise is expected to increase as the temperature decreases. We perform the measurement at 10, 100, 150, 200, 250, 300, 400, and 500 mK to observe the temperature-dependent behavior of the TLS noise. Figure 4.12 shows that the frequency noise PSD decreases with increasing temperature. At 500 mK, we can also see the white noise floor after 0.1 Hz.

According to the prediction of the tunneling model, $S_y \sim T^{-(1-\mu)}$. The phenomenological parameter μ derived from most of the SAW modes are $\mu \approx 0.2-0.4$, which are in the same range as the other experiments [5, 21, 22]. Figure 4.13 shows examples of the frequency noise $S_y(0.1 \text{ Hz})$ of mode #7 to #9, which give $\mu \approx 0.2 - 0.3$.

Furthermore, we investigate the correlation of the frequency noises at different detunings as a function of the temperature. The examples of the temperature dependence of the correlation coefficients are illustrated in Figure 4.14. The correlations decrease as the temperature increases. Remarkably, the correlation coefficients are high for all detunings at the temperature of 250 mK, which is unexpected.

4.3 Exploring the local effects of the TLSs

To study the local effects of the TLSs at the nearby frequency, we pump the SAW resonator using different configurations and compare the correlation between the modes. All measurements are performed using input power -47 dBm. The record

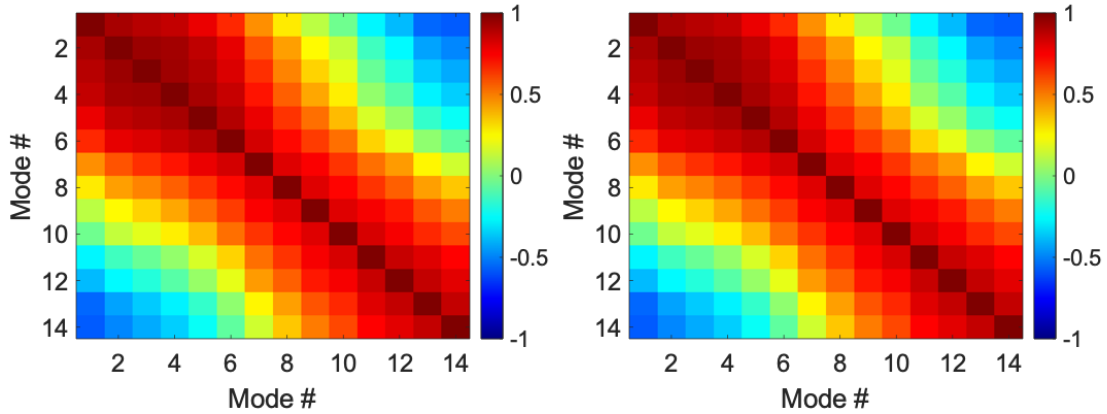


Figure 4.7: (Left) The matrix showing the correlation coefficients of phase and (right) the resonance frequency shifts.

length is 7 hours 15 minutes, with a sampling rate of 10 Hz. The driven mode numbers in each measurement are summarized in Table 4.1.

Configuration	Driven resonance mode #
1	1,2,3, ..., 14
2	1,4,7,10,13
3	1,5,9,13
4	1,14

Table 4.1: A summary of the mode number driven in each configuration.

Figure 4.15 shows the correlation coefficient as a function of detuning. As observed in the previous analysis, the correlation coefficient of the resonance frequency shifts decreases as the detuning increases. In this experiment, we find that the magnitude of the correlation coefficients between mode #1 and the other modes reduces as the number of driven mode decreases. One of the possible reasons is that the total number of phonons in the resonator is less when we drive a fewer number of modes. This agrees with the result in the previous section, showing that the correlations between modes reduce as the number of phonons decreases. Therefore, there is less number of saturated TLSs. As a result, the resonator is less affected by the TLS coupling.

An important remark from this analysis is that the correlation between mode #1 and mode #14 show negative values in both configuration 1 and 2. However, since the number of phonons in each case are not comparable, the correlations between the noise cannot be directly compared.

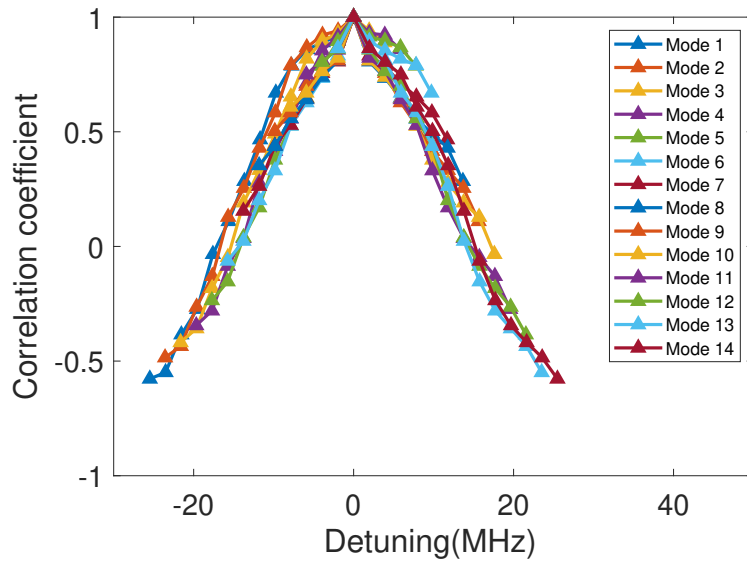


Figure 4.8: The correlation coefficients of resonance frequency shift, Δf_r , as a function of detuning. Note that all the data seem to collapse to a single line. Also, note the change in sign when the detuning is about ± 18 MHz.

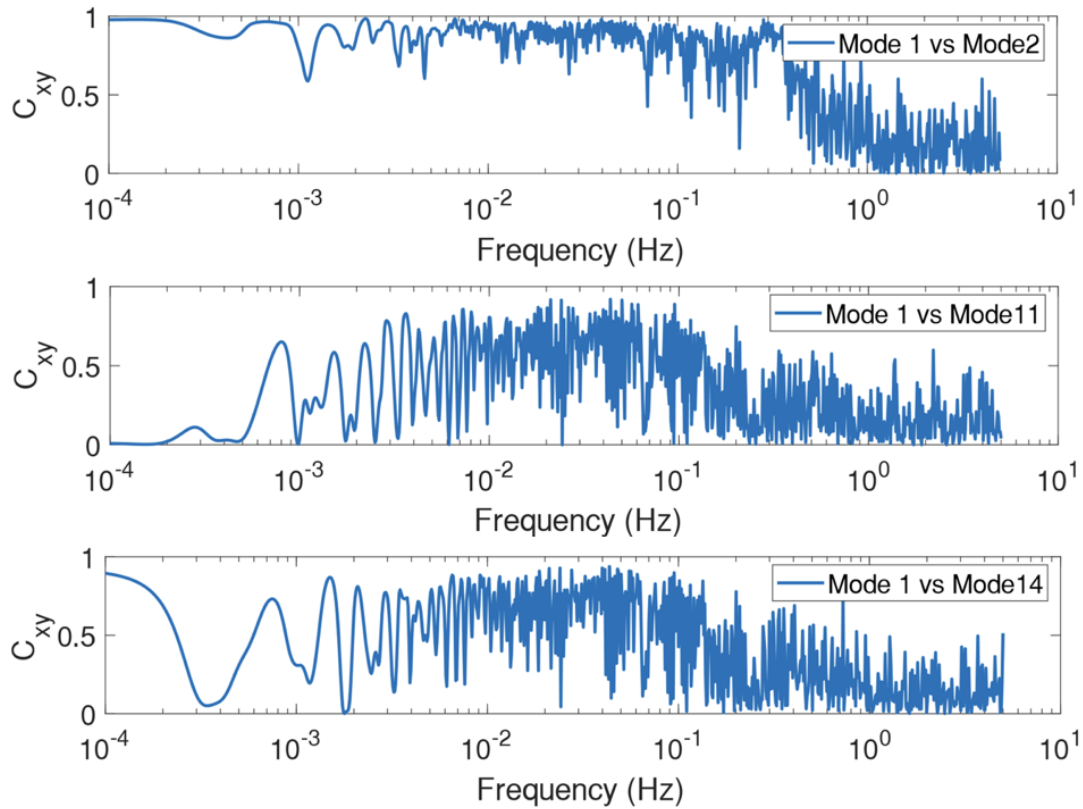


Figure 4.9: Magnitude-squared coherence of the resonance frequency shift Δf_r between mode #1 and (top) mode #2, (middle) mode #11, and (bottom) mode #14.

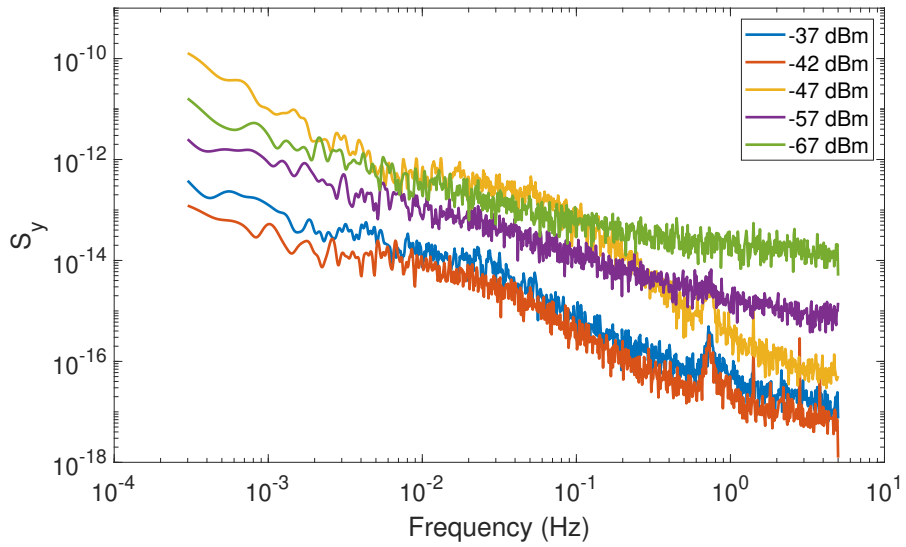


Figure 4.10: The power dependence of the frequency noise from mode #8 at the temperature of 10 mK.

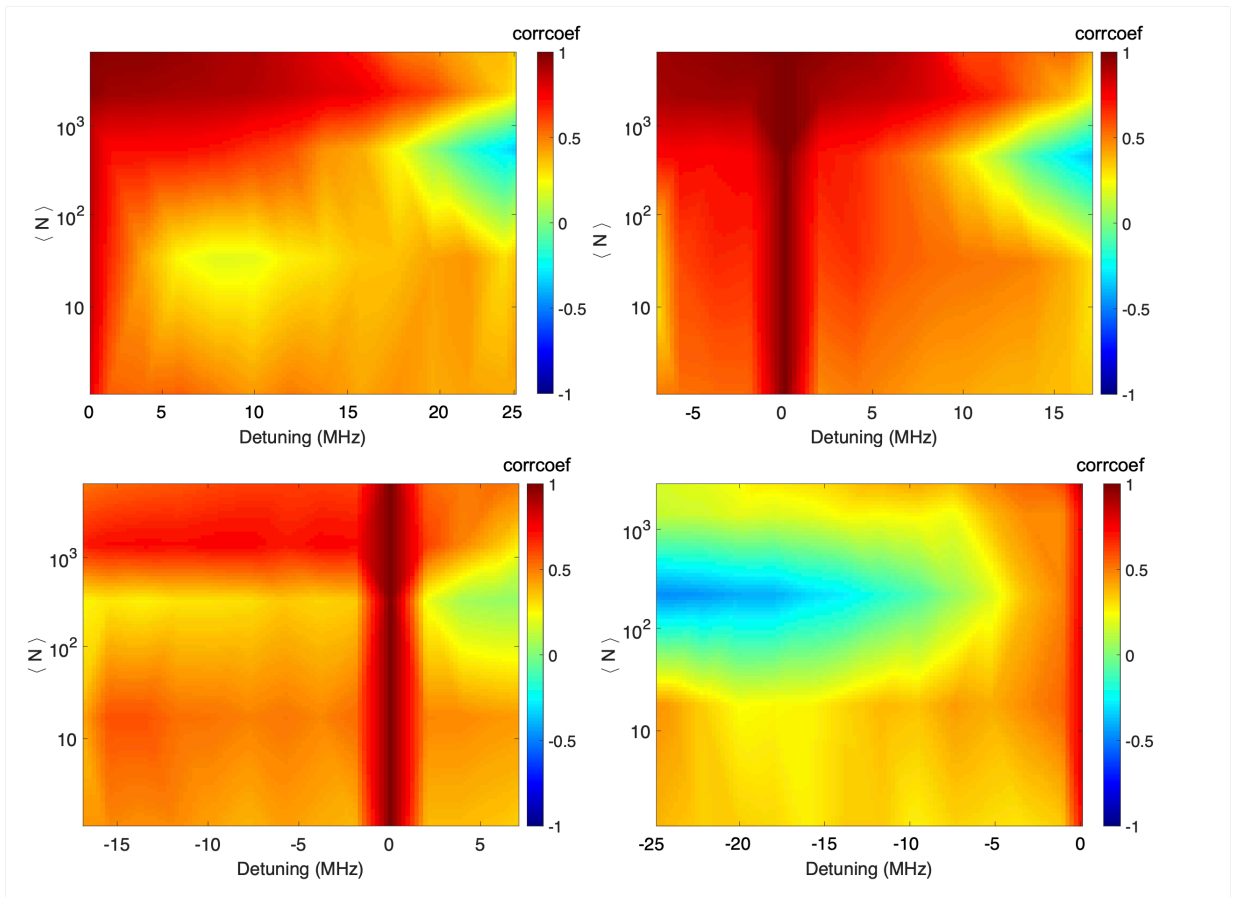


Figure 4.11: The correlation coefficients of the resonance frequency shifts derived from (top left) mode #1, (top right) mode 5, (bottom left) mode #10 and (bottom right) mode #14 with the other modes as a function of estimated number of phonons $\langle N \rangle$ and detuning.

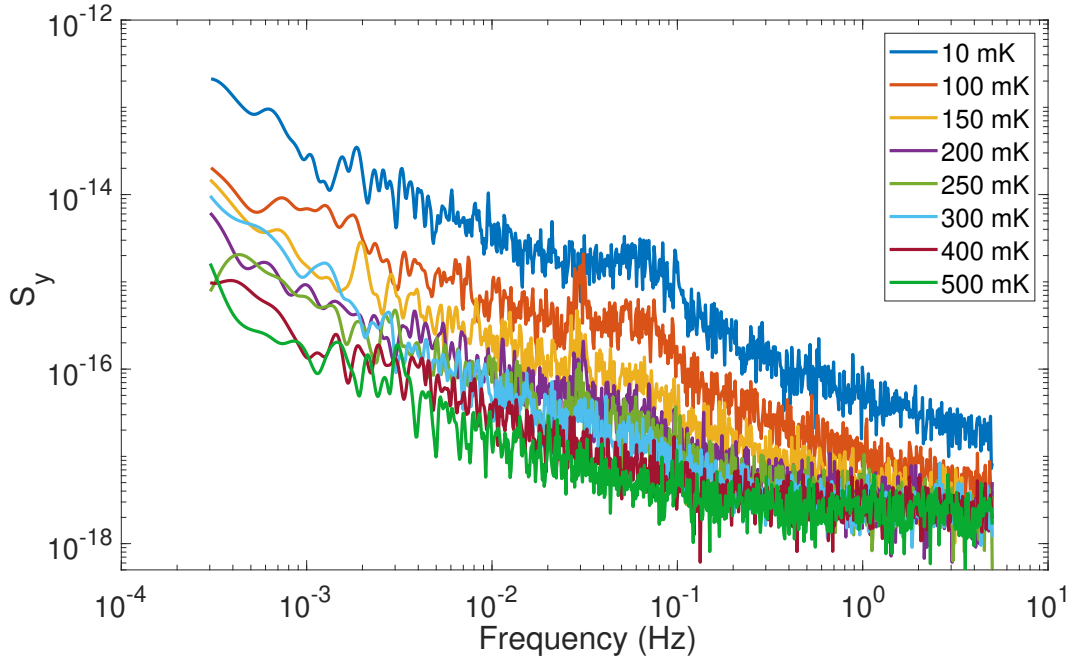


Figure 4.12: An example of Welch power spectral density of Δf_r of mode #8 at different temperatures.

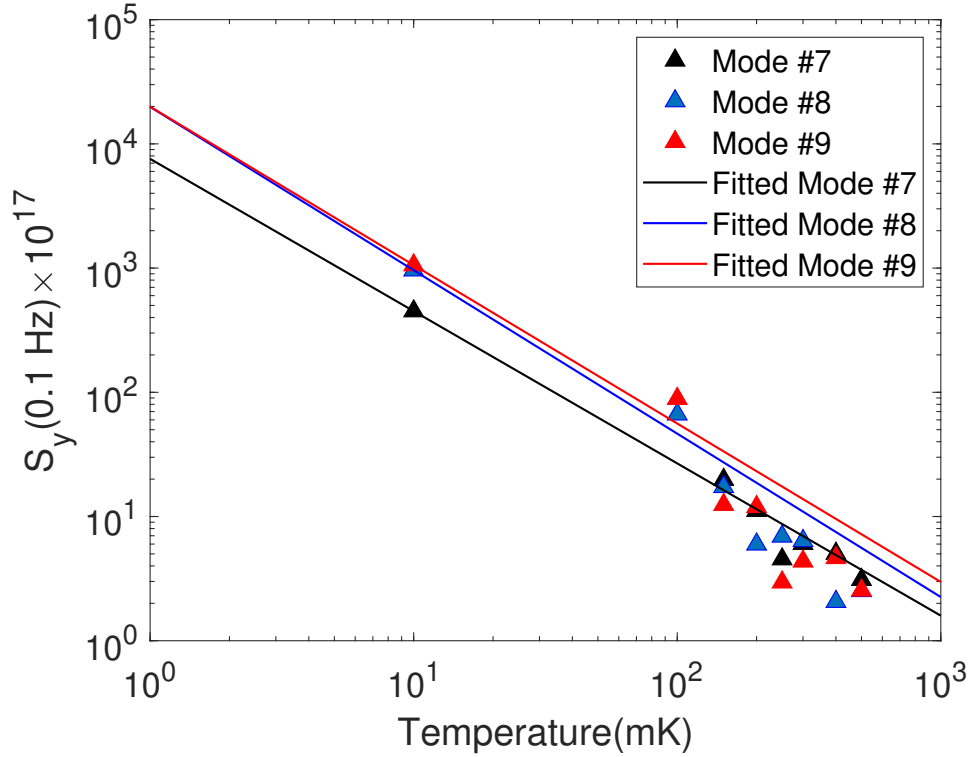


Figure 4.13: Temperature dependent of the frequency noise from mode #7 to #9. The data are fitted to $S_y \sim T^{-(1+\mu)}$. We get $\mu = \{0.28, 0.32, 0.23\}$ for mode #7, #8, #9, respectively.

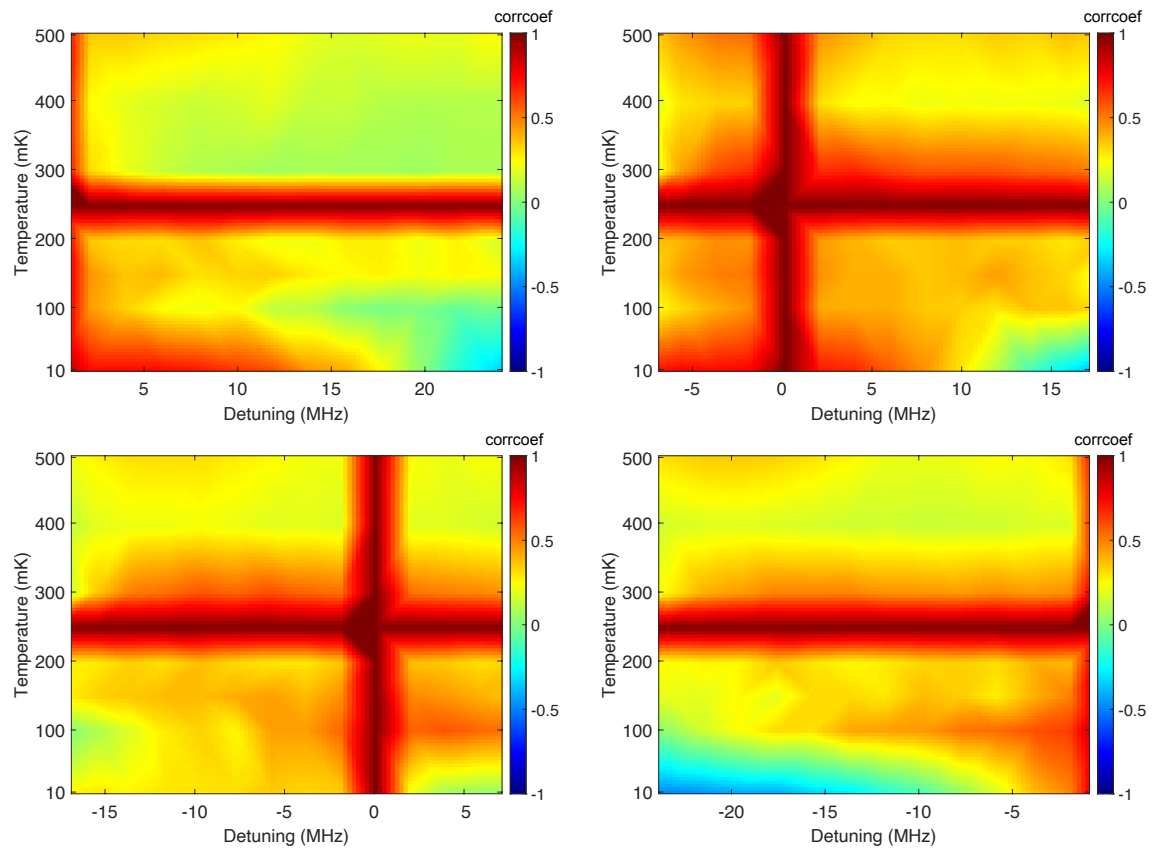


Figure 4.14: The correlation coefficients of the resonance frequency shifts derived from (top left) mode #1, (top right) mode #5, (bottom left) mode #10 and (bottom right) mode #14 with the other modes as a function of temperature and detuning.

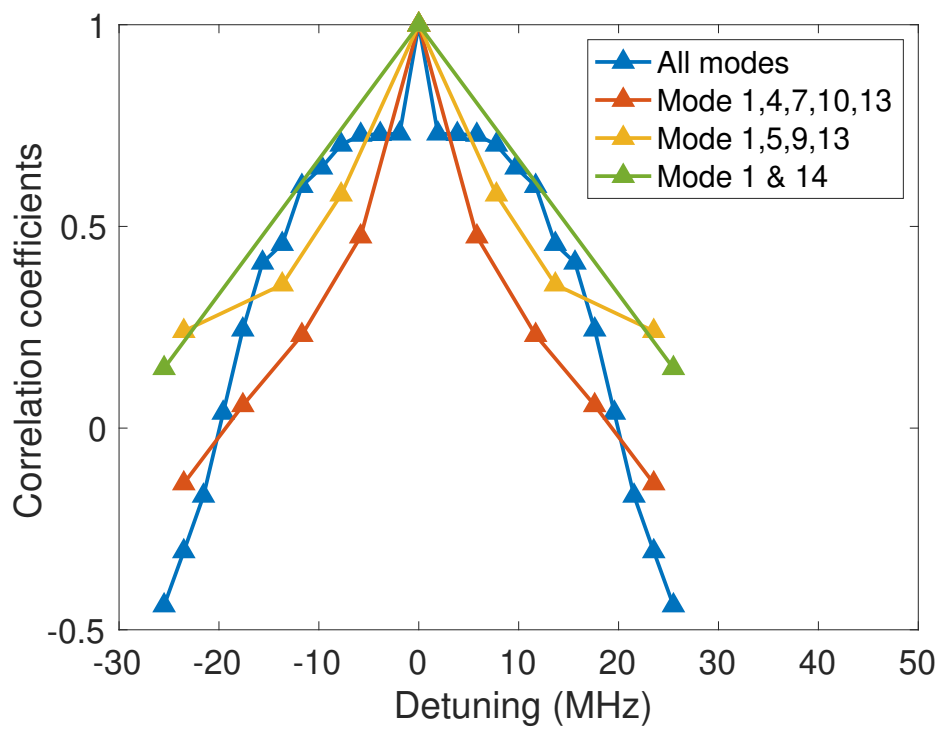


Figure 4.15: The correlation coefficients of the resonance frequency shifts as a function of detuning when driving different number of tones in the SAW resonator.

5

Conclusion

We measure phase noise caused by TLSs at many resonance frequencies of a SAW resonator simultaneously. The phase noise data are converted to resonance frequency shifts. The power spectral density of the frequency noise reveals that there is a Lorentzian noise from a single dominant TLS, in addition to the well-known $1/f$ spectrum. The magnitude-squared coherence suggests that the noise from different modes are correlated in the frequency range that shows the $1/f$ characteristic. Therefore, we can argue that the noise caused by TLSs are correlated. The correlation of the noise can be explained by the fact that each SAW mode coupling to the same TLS ensemble. The correlation coefficients of the TLS noise diminish with increasing detuning, which is in agreement with the prediction of the TLS model. The striking result is that, as the detuning increases, the correlation coefficient decreases until zero and becomes negative, suggesting that the noise of two different modes correlate in the opposite manner. The negative correlations cannot be explained by the current model.

Additionally, the frequency noise correlations are power and temperature-dependent. We found that the correlations of the frequency noise are high when there is an effect of a single dominant TLS presented. Although many previous experiments have reported the power and temperature-dependence of the noise spectra, the relationship of the noise between different modes has not been studied. Therefore, further investigations beyond this work are required, both experiment and theory.

As discussed, the physics governing the relationships of the frequency noise has not been completely understood. It would be interesting to investigate how the correlation changes with larger detuning. The result could suggest the distribution of the TLSs and give a better insight into their coupling mechanism.

Bibliography

- [1] F. Arute, K. Arya, R. Babbush, D. Bacon, J.C. Bardin, R. Barends, R. Biswas, S. Boixo, F.G.S.L. Brandao, D.A. Buell, B. Burkett, Y. Chen, Z. Chen, B. Chiaro, R. Collins, W. Courtney, A. Dunsworth, E. Farhi, B. Foxen, ..., J.M. Martinis. Quantum supremacy using a programmable superconducting processor. *Nature* **574**.7779 (2019), 505-511.
- [2] J.M. Martinis, K.B. Cooper, R. McDermott, M. Steffen, M. Ansmann, K.D. Osborn, K. Cicak, S. Oh, D.P. Pappas, R.W. Simmonds, and C.C. Yu. Decoherence in Josephson qubits from dielectric loss. *Physical Review Letters* **95**.21 (2015), 210503.
- [3] L. Faoro, and L.B. Ioffe. Internal Loss of Superconducting Resonators Induced by Interacting Two-Level Systems. *Physical Review Letters* **109**.15 (2012), 157005.
- [4] C. Müller, J.H. Cole, and J. Lisenfeld, Towards understanding two-levels-systems in amorphous solids: insights from quantum circuits. *Reports in Progress in Physics* **82** (2019), 124501.
- [5] J. Burnett, L. Faoro, I. Wisby, V.L. Gurtovio, A.V. Chernykh, G.M. Mikhailov, V.A. Tulin, R. Shaikhaidarov, V. Antonov, P.J. Meeson, A.Y. Tzalenchuk, and T. Linström. Evidence for interacting two-level systems from the $1/f$ noise of a superconducting resonator. *Nature Communication* **5** (2014), 4119.
- [6] C.H.W. Barnes, J.M. Shilton, and A.M. Robinson. Quantum computation using electrons trapped by a surface acoustic waves. *Physical Review B* **62** (2000), 12.
- [7] M.V. Gustafsson, T. Aref, A.F. Kockum, M.K. Ekström, G. Johansson, and P. Delsing. Propagating phonons coupled to an artificial atom. *Science* **346** (2014), 207.
- [8] R. Manenti, A.F. Kockum, A. Patterson, T. Behrle, J. Rahamim, G. Tancredi, F. Nori, and P.J. Leek. Circuit quantum acoustodynamics with surface acoustic waves. *Nature Communications* **8** (2017), 975.
- [9] R. Manenti, M.J. Peterer, E.B. Magnusson, A. Patterson, and P.J. Leek. Surface acoustic wave resonators in the quantum regime. *Physical Review B* **93** (2016), 041411.
- [10] G. Andersson, A.L.O. Bilobran, M. Scigliuzzo, M.M. de Lima, J.H. Cole, and P. Delsing. Acoustic spectral hole-burning in a two-level system ensemble. *Arxiv: 2002.09308v1* (2020).
- [11] P. W. Anderson, B. I. Halperin, and C. M. Varma. Anomalous low-temperature thermal properties of glasses and spin glasses. *Philosophical Magazine* **25**.1 (1972), 1-9.

- [12] W.A. Phillips, Tunneling states in amorphous solids. *Journal of Low Temperature Physics* **7** (1972), 351–360.
- [13] J. Gao, M. Daal, A. Vayonakis., S. Kumar, J. Zmuidzinas, B. Sadoulet, B.A. Mazin, P.K. Day, and H.G. Leduc. Experimental evidence for a surface distribution of two-level systems in superconducting lithographed microwave resonators. *Applied Physics Letter* **92** (2008), 152505.
- [14] D. P. Pappas, M. R. Vissers, D. S. Wisbey, J. S. Kline, and J. Gao, Two Level System Loss in Superconducting Microwave Resonators. *IEEE Transactions on Applied Superconductivity* **21** (2011), 871.
- [15] D. V. Anghel, T. Kühn, Y. M. Galperin, and M. Manninen. Interaction of two-level systems in amorphous materials with arbitrary phonon fields. *Physical Review B* **75** (2007), 064202.
- [16] J. Lisenfeld, G. Grabovskij, C. Müller, J.H. Cole, G. Weiss, and A.V. Ustinov. Observation of directly interacting coherent two-level systems in an amorphous material. *Nature Communication* **6** (2015), 6182.
- [17] G. Andersson. *Quantum acoustics with superconducting circuits*. PhD thesis. Chalmers University of Technology, 2020.
- [18] L. Faoro and L.B. Ioffe. Interacting tunneling model for two-level systems in amorphous materials and its predictions for their dephasing and noise in superconducting microresonators. *Physical Review B* **91** (2015), 014201.
- [19] J. Gao, J. Zmuidzinas, B.A. Mazin, H.G. LeDuc, and P.K. Day. Noise properties of superconducting coplanar waveguide microwave resonator. *Applied Physics Letter* **90** (2007), 102597.
- [20] J.L. Black and B.I. Halperin. Spectral diffusion, phonon echoes, and saturation recovery in glasses at low temperatures. *Physical Review B* **69** (1977), 2879-95.
- [21] J. Burnett, L. Faoro, and T. Linström. Analysis of high quality superconducting resonators: consequence for TLS properties in amorphous oxides. *Superconductor Science and Technology* **29** (2016), 044008.
- [22] A.L. Burin, A. Matityahu, and M. Schechter. Low-temperature 1/f noise in microwave dielectric constant of amorphous dielectrics in Josephson qubits. *Physical Review B* **92** (2015), 174201.
- [23] J. Burnett, A. Bengsston, D. Niepce, and J. Bylander. Noise and loss of superconducting aluminium resonators at single photon energies. *IOP Conference Series of Journal of Physics: Conference Series* **969** (2018), 012131.
- [24] S. Takei, V.M. Galitski, and K.D. Osborn. Squeezed noise due to two-level system defects in superconducting resonator circuits. *Physical Review B* **85** (2012), 104507.
- [25] J. Gao, M. Daal, J.M. Martinis, A. Vayonakis, J. Zmuidzinas, B. Sadoulet, B.A. Mazin, P.K. Day, and H.G. Leduc. A semiempirical model for two-level system noise in superconducting microresonators. *Applied Physics Letter* **92** (2008), 212504.
- [26] D.P. Morgan. *Surface Acoustic Wave Filters: With Applications to Electronic Communications and Signal Processing*. Academic Press, 2010.
- [27] Standford Research Systems (2020, 2 July). About lock-in amplifier - Application Note 3. Retrieved from <https://www.thinksrs.com/downloads/pdfs/applicationnotes/AboutLIAs.pdf>.

-
- [28] M. Ankel. *Building a Microwave Multifrequency Modulation Setup*. Master's thesis. Chalmers University of Technology, 2019.
- [29] Intermodulation (2020, June 25). User Manual - Intermodulation AFM Software Suite. Retrieved from https://www.intermodulation-products.com/manuals/IMP-MLA_user_manual/mla.html.
- [30] S.E. de Graff, L. Faoro, J. Burnett, A.A. Adamyam, A. Ya. Tzalenchuk, S.E. Kubatkin, T. Linström, and A.V. Danilov. Suppression of low-frequency charge noise in superconducting resonators by surface spin desorption. *Nature Communications* **9** (2018), 1143.
- [31] S. Probst, S.B. Song, P.A. Bushev, A.V. Ustinov, and M. Weides. Efficient and robust analysis of complex scattering data under noise in microwave resonators. *Review of Scientific Instrument* **86** (2015), 024706.
- [32] J. A. Nelder and R. Mead. A Simplex Method for Function Minimization. *The Computer Journal* **7.4**, (1965), 308–313.
- [33] N. Kirch, E. Svetitsky, A.L. Burin, M. Schechter and N. Katz. Supplementary materials to "Revealing the nonlinear response of tunneling two-level systems ensemble using coupled modes". *Physical Review Materials* **1** (2017), 012601.
- [34] M. Aspelmeyer, T.J. Kippenberg, and F. Marquardt, Cavity optomechanics. *Reviews of Modern Physics* **86** (2014), 1391.
- [35] J. J. Burnett, A. Bengtsson, M. Scigliuzzo, D. Niepce, M. Kudra, P. Delsing, and J. Bylander. Decoherence benchmarking of superconducting qubits. *npj Quantum Information* **5.54** (2019).
- [36] E. Rubiola. *Phase Noise and Frequency Stability in Oscillators*. Cambridge University Press, 2008.
- [37] W.D. Penny. *Signal Processing Course*. University College London, 2000.
- [38] W.A. Gardner. A unifying view of coherence in signal processing. *Signal Processing* **29** (1992), 113-140.
- [39] J. Burnett, T. Linström, M. Oxborrow, Y. Harada, Y. Sekine, P. Meeson, and A. Y. Tzalenchuk. Slow noise processes in superconducting resonators. *Physical Review B* **87** (2013), 140501.
- [40] C. Müller, J. Lisenfeld, A. Schirman, and S. Poletto. Interacting two-level defects as sources of fluctuating high-frequency noise in superconducting circuits. *Physical Review B* **92** (2015), 035442.
- [41] R. Barends, N. Vercrayssen, A. Endo, P.J. de Visser, T. Zijlstra, T.M. Klapwijk, and J.J.A. Baselmans. Reduced frequency noise in superconducting resonators. *Applied Physics Letters* **97** (2010), 033507.
- [42] S. Kumar, J. Gao, J. Zmuidzinas, B.A. Mazin, H.G. LeDuc, and P.K. Day. Temperature dependence of the frequency and noise of superconducting coplanar waveguide resonators. *Applied Physics Letter* **92** (2008), 123503.

A

MLA setup

A.1 Intermodulation software

Intermodulation is a graphic user interface for operating the multi-frequency lock-in amplifier (MLA). The software requires python3. It is recommended to use Anaconda or miniconda platform. To execute the program, the following packages are mandatory:

- numpy
- scipy
- paramiko
- configobj
- ipython
- wxpython
- matplotlib
- h5py
- scikit-learn
- cython

A.2 MLA setup

The default IP address of the MLA box is 192.168.42.50. To connect the box with the lab network, one may have to re-assign a new IP address to the box. This can be done by connecting MLA to a local computer via an ethernet port and executing the command below from the python shell window in Intermodulation software.

```
1 setup.set_ip_address( NEW_IP , 192 .168.42.50 )
```

After changing the IP address of the box, one has to edit the IP address setting under 'communication' in a configuration file mla_config.ini. Reboot MLA and relaunch the software.

B

Scripts for measurements

This section includes python scripts for operating the MLA. These scripts are executed on the Intermodulation software.

B.1 Frequency sweeping

A script to frequency sweep for SAW resonator characterization.

```
1 import numpy as np
2 import csv as csv
3 from datetime import datetime
4 from scipy.optimize import minimize
5
6 def FrequencySweep_Lockin_Norm (drive_amp, scaling_amp_array, fcenter, amp_sweep)
  ↪ :
7     import numpy as np
8     amp_array = []
9     phase_array = []
10    inputamp_array = []
11
12 # User parameters
13    f_Mhz = np.linspace(50, 80, 30000) #30001
14    dummy = 50
15    dummy_array = np.append(dummy, fcenter)
16    df = np.ones_like(dummy_array) * 1000.0 # Hz
17    avg = 1
18    phases = np.ones_like(dummy_array) * 0.0
19    out_1_mask = np.ones_like(dummy_array)
20    out_2_mask = np.ones_like(dummy_array) * 0.0
21    scaling_amp_array = np.array(scaling_amp_array)
22    scaled_drive_amp_array =drive_amp * scaling_amp_array
23    amp_lockin = np.multiply(np.ones_like(fcenter) ,scaled_drive_amp_array)
24    ampls = np.append(amp_sweep,amp_lockin)
25
26 # Save data
27    freq_array = f_Mhz*1e6
28    mag = np.log10(drive_amp)
29    path = r"C:\Users\qtlab\Desktop\Pias\2020_07_03\20
  ↪ _07_03_LockIn_FrequencySweep_Norm_Amp_"
30    name = path + str(mag) + r'.txt'
31
32 # Setup MLA
33    #mla.lockin.set_df(df)
34    mla.lockin.set_output_mask(out_1_mask, port=1)
```

B. Scripts for measurements

```
35 mla.lockin.set_output_mask(out_2_mask, port=2)
36 mla.lockin.set_phases(phases, 'degree')
37 mla.lockin.set_amplitudes(ampls)
38
39 # Allocate memory for result
40 amps = np.zeros_like(f_Mhz)
41 amps[:] = np.NaN
42 phases = np.zeros_like(f_Mhz)
43 phases[:] = np.NaN
44 inputamp = np.zeros_like(f_Mhz)
45 inputamp[:] = np.NaN
46
47 # Setup GUI
48 main.gui.show_panel(main.scriptplot)
49
50 # Initialize plots
51 scriptplot.fig.clear() # remove if you want multiple sweeps in one plot
52 ax = scriptplot.fig.add_subplot(2, 1, 1)
53 ax.set_xlabel('Frequency [MHz]')
54 ax.set_ylabel('Amplitude [V]')
55 ax.set_title('Frequency sweep')
56 ax.set_xlim([f_Mhz.min(), f_Mhz.max()])
57 line = ax.plot(f_Mhz, amps)[0]
58
59 exp = scriptplot.fig.add_subplot(2, 1, 2)
60 exp.set_xlabel('Frequency [MHz]')
61 exp.set_ylabel('Phase [rad]')
62 exp.set_xlim([f_Mhz.min(), f_Mhz.max()])
63 linep = exp.plot(f_Mhz, phases)[0]
64
65 # Start lockin should have cluster_size=1
66 # since we do not want many packages buffered
67 # on MLA before they are transmitted
68 mla.lockin.start_lockin(cluster_size=1)
69 t0 = time.time()
70 for ii, f in enumerate(f_Mhz):
71     # Set parameters in loop
72     f = f*1e6
73     f_lockin = np.append(f, fcenter)
74     f_tuned, df_tuned = mla.lockin.tune1(f_lockin, df)
75     f_Mhz[ii] = f_tuned[0] * 1e-6
76     mla.lockin.set_df(df_tuned, wait_for_effect=False)
77     mla.lockin.set_frequencies(f_tuned, idx='all', wait_for_effect=True) #
78     ↪ wait for effect on last MLA setting
79
80     # Recieve new lockin data
81     mla.lockin.wait_for_new_pixels(avg)
82     pix, meta = mla.lockin.get_pixels(avg)
83     pix = np.mean(pix, axis = 1)
84     amps[ii] = np.abs(pix[0])
85     phases[ii] = np.angle(pix[0])
86     inputamp[ii] = drive_amp
87
88 # Plot graph
89 if not scriptplot.is_drawing:
90     scriptplot.is_drawing = True
```

```

90     line.set_data(f_Mhz[:ii + 1], amps[:ii + 1])
91     linep.set_data(f_Mhz[:ii + 1], phases[:ii + 1])
92     scriptplot.autoscale_y(ax)
93     scriptplot.autoscale_y(axp)
94     wx.CallAfter(scriptplot.draw)
95     if not scriptpanel.is_running:
96         break
97
98     # Collect data: amps[ii] and phase[ii]
99
100     a = np.append(f, amps[ii])
101     a = np.append(a, phases[ii])
102     a = np.append(a, inputamp[ii])
103     a = np.reshape(a, (1,4))
104     with open(name, "a") as Output:
105         np.savetxt(Output, a, delimiter=",", fmt='%s')
106     t1 = time.time() - t0
107     print('Run time: ' + str(t1))
108     mla.lockin.stop_lockin()
109
110 # Final update of plots
111     line.set_data(f_Mhz, amps)
112     linep.set_data(f_Mhz, phases)
113     scriptplot.autoscale_y(ax)
114     scriptplot.autoscale_y(axp)
115     wx.CallAfter(scriptplot.draw)
116     filename = scriptutils.generate_filename() + '.png'
117     wx.CallAfter(scriptplot.fig.savefig, filename)
118
119
120 # Execution
121
122 amp_scaling_array =
123     ↪ [0.973514702, 1.01151613, 1.017694345, 0.999641672, 1, 0.974050566, 0.973985249,
124     0.960021593, 0.95457614, 0.95349909, 0.957527383, 0.943180891, 0.941541893,
125     0.982418008]
126 fcenter = [53224107.4702490, 55135171.1723724, 57079235.9745325, 59033301.1100370,
127     60994366.4788826, 62956431.8810627, 64923497.4499150, 66890563.0187673,
128     68859628.6542885, 70828694.2898097, 72799759.9919997, 74769825.6608554,
129     76741891.3963799, 78711957.0652355]
130 FrequencySweep_Lockin_Norm (10**(-1.0), amp_scaling_array, fcenter, 10**(-1.5))
131 print('Finished all measurements')

```

B.2 Amplitude optimization

An optimization code for determining f_{probe} , where the amplitude is minimum.

```

1 import numpy as np
2 import csv as csv
3 from datetime import datetime
4 from scipy.optimize import minimize
5

```

B. Scripts for measurements

```
6 def mean_output_amp_MultiModes(offset_array, fmode_array, drive_amp,
  ↳ scaling_amp_array, wanted_df, Navg ,lockin):
7
8     fcenter_array = fmode_array + offset_array
9     out_1_mask = np.ones_like(fcenter_array)
10    out_2_mask = np.zeros_like(fcenter_array)
11    lockin.set_output_mask(out_1_mask, port=1)
12    lockin.set_output_mask( out_2_mask, port=2)
13    phases = np.zeros_like(fcenter_array)
14    df = np.ones_like(fcenter_array)*wanted_df
15    pump_amp_array = np.ones_like(fcenter_array) *drive_amp
16
17    pump_amp = np.multiply(pump_amp_array,scaling_amp_array)
18    lockin.set_phases(phases, 'degree')
19    lockin.set_amplitudes(pump_amp)
20
21    f_tuned, df_tuned = lockin.tune1(fcenter_array, df, priority='f')
22    lockin.set_df(df_tuned, wait_for_effect=False)
23    lockin.set_frequencies(f_tuned, idx='all', wait_for_effect=True) # wait for
  ↳ effect on the last MLA setting
24    lockin.start_lockin(cluster_size=1)
25    lockin.wait_for_new_pixels(Navg)
26    pixels, meta = lockin.get_pixels(Navg)
27    pix = np.mean(pixels, axis = 1)
28    sum_amp_out = 0
29
30    for i in range (0,len(fcenter_array)):
31        Amp = np.abs(pix[i])*np.abs(pix[i])
32        sum_amp_out = sum_amp_out+ Amp
33
34    return sum_amp_out
35
36
37 def optimizer(fcenter,scaling_amp_array,A):
38     # Setup GUI
39     main.gui.show_panel(main.scriptplot)
40     print('Running Optimization')
41     Navg = 10
42     wanted_df = 100
43     offset = 5e3
44     offset_array = np.ones((len(fcenter)-1))*offset # When perform optimization
  ↳ using several modes
45     f_offset = [0]
46     for i in range(1,len(fcenter)):
47         f_offset1 = minimize(mean_output_amp_MultiModes,offset_array[i-1], args =
  ↳ (fcenter[i],A,scaling_amp_array[i-1],wanted_df, Navg,mla.lockin), method
  ↳ = 'Nelder-Mead', options = {'maxfev': 1000})
48         print('fcenter =',fcenter[i])
49         print('scaling =',scaling_amp_array[i-1])
50         print(f_offset1)
51         f_offset = np.append(f_offset,f_offset1.x )
52         print(f_offset)
53
54     fcenter = np.array(fcenter)
55     f_offset = np.array(f_offset)
56     finalf = fcenter + f_offset
```

```

57 finalf = finalf.tolist()
58 print('final offset = ', f_offset.tolist())
59 print('final freq = ', finalf)
60
61 return finalf

```

B.3 Phase noise measurement

A script for performing lock-in frequencies and measure S_{11} time trace.

```

1 def TimeTraceMeasurement_Norm_WithOptimizer(fcenter, scaling_amp_array, A, nop):
2     amp_array = []
3     phase_array = []
4     time_array = []
5
6     print("Measuring =", len(fcenter), "modes simultaneously")
7
8     # Configure lockin
9     df = np.ones_like(fcenter) * 100.0 # Hz
10
11     phases = np.ones_like(fcenter) * 0.0
12     drive_amp = np.ones((1, len(fcenter)-1)) * A
13     out_1_mask = np.ones_like(fcenter)
14     out_2_mask = np.ones_like(fcenter) * 0.0
15     avg = 10
16     amp_lockin = np.multiply(drive_amp, scaling_amp_array)
17     ampls = np.append(A, amp_lockin)
18
19     # Program MLA
20     mla.lockin.set_output_mask(out_1_mask, port=1)
21     mla.lockin.set_output_mask(out_2_mask, port=2)
22     mla.lockin.set_phases(phases, 'degree')
23     mla.lockin.set_amplitudes(ampls)
24
25     # Setup GUI
26     main.gui.show_panel(main.scriptplot)
27
28 # Save data
29 mag = np.log10(ampls[0])
30 path = r"C:\Users\qtlab\Desktop\Pias\2020_07_11\2020
31     ↪ _07_11_TimeTrace_MultiModes_Norm_Optimized_Amp"+str(mag)
32     name = path + '_' + str(len(scaling_amp_array)) + r'Modes.csv'
33
34     # Allocate memory for result
35     times = np.zeros((1,1))
36     times[:] = np.NaN
37     amps = np.zeros((1, len(fcenter)))
38     amps[:] = np.NaN
39     phases = np.zeros((1, len(fcenter)))
40     phases[:] = np.NaN
41
42     # Make lockin measurement
43     f_tuned, df_tuned = mla.lockin.tune2(fcenter, df, priority='f')
44     print('f_tuned: ' + str(f_tuned/1e6))

```

B. Scripts for measurements

```
44
45 mla.lockin.set_df(df_tuned, wait_for_effect=True)
46 mla.lockin.set_frequencies(f_tuned, idx='all', wait_for_effect=True) # wait
↳ for effect on last MLA setting
47 mla.lockin.start_lockin(cluster_size=1)
48
49 # Record lockin frequency
50 path1 = r"C:\Users\qtlab\Desktop\Pias\2020_07_11\2020
↳ _07_11_MeasurementParameters_Norm_Optimized_Amp"+str(mag)
51 name1 = path + '_' + str(len(scoring_amp_array)) + r'Modes.csv'
52
53 f_tuned_save = np.reshape(f_tuned, (1, len(f_tuned)))
54 ampls = np.reshape(ampls, (1, len(ampls)))
55 final_params = np.concatenate((f_tuned_save, ampls), axis=1)
56 with open(name1, "a") as Output1:
57     np.savetxt(Output1, final_params, delimiter=",", fmt='%s')
58
59 t0 = time.time()
60 i = 0
61 while i < nop+1:
62     # Recieve new lockin data
63     mla.lockin.wait_for_new_pixels(avg)
64     pixels, meta = mla.lockin.get_pixels(avg)
65     pix = np.mean(pixels, axis = 1)
66     for j in range (0, len(fcenter)):
67         amps[0, j] = np.abs(pix[j])
68         phases[0, j] = np.angle(pix[j])
69     t2 = time.time() - t0
70     times[0] = t2
71     if np.mod(i, 1e2) == 0:
72         print('Data collected: ' + str(i))
73
74     # Collect data: amps[i] and phase[i]
75     times_save = times[0]
76     amps_save = amps[0, :]
77     phases_save = phases[0, :]
78     times_save = np.reshape(times_save, (1, 1))
79     amps_save = np.reshape(amps_save, (1, len(fcenter)))
80     phases_save = np.reshape(phases_save, (1, len(fcenter)))
81
82     now = datetime.now()
83     t_stamp = now.strftime('%Y/%m/%d, %H:%M:%S')
84     t_stamp = np.reshape(t_stamp, (1, 1))
85
86     # print(np.shape(phases_save))
87     a = np.concatenate((t_stamp, times_save, amps_save, phases_save), axis=1)
88     with open(name, "a") as Output:
89         np.savetxt(Output, a, delimiter=",", fmt='%s')
90     i = i+1
91     print('Finished one measurement.')
92
93
94 # Execution for time trace measurement
95
96 scaling_amp_array = [0.973514702, 1.01151613, 1.017694345, 0.999641672, 1,
↳ 0.974050566, 0.973985249, 0.960021593, 0.95457614, 0.95349909,
```

```
    ↪ 0.957527383, 0.943180891 ,0.941541893, 0.982418008]
97 fcenter = [70000000.0, 53205661.03515625, 55116887.50143051, 57061918.75119209,
    ↪ 59015920.96977234, 60977275.01525879, 62939899.99809265, 64906753.90625,
    ↪ 66874287.5, 68845819.20347214, 70813512.2549057, 72783831.25, 74754237.5,
    ↪ 76726150.0, 78687000.0]
98
99 fcenter_opt = optimizer(fcenter, scaling_amp_array,10**(-1.0))
100 TimeTraceMeasurement_Norm_WithOptimizer(fcenter_opt, scaling_amp_array,10**(-1.0)
    ↪ , 2.6e5)
```


C

Supplementary data

C.1 Long measurement

Phase noise measurement is performed for 24 hours, using -47 dBm input drive. The number of points is 4.32×10^5 . The sampling rate is 10 Hz, similar to the previous measurements. The time traces illustrated in Figure C.1 - C.3 shows explicit correlations of the amplitude, phase, and resonance frequency fluctuations except the last four modes.

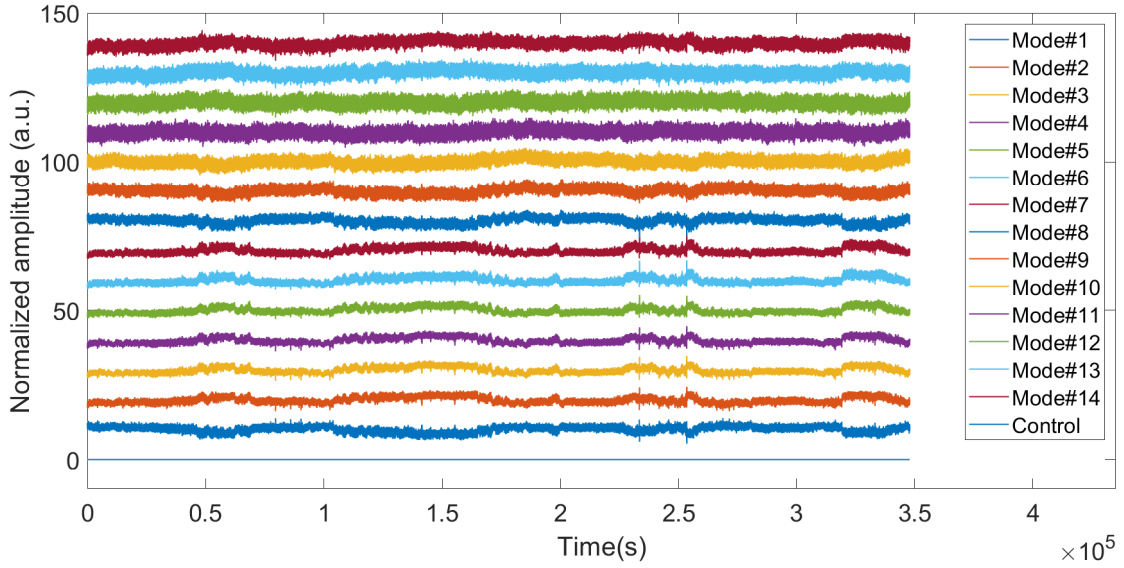


Figure C.1: The time traces of the measured amplitudes. The bottom trace represents the control tone measured at 2.39 GHz, which is off-resonance with the SAW modes.

The power spectral density and the Allan deviation displayed in Figure C.7 suggest the presence of a single dominant TLS, which results in the Lorentzian noise characteristics. Due to the long measurement time, we can capture the longer time processes than that in the measurement discussed in Chapter 4. The black line in the PSD plot represents the fitted data using $S_y(f) = \frac{A\gamma}{(f^2 + \gamma^2)} + \frac{h_{-1}}{f}$. The result shows $A = 3.39 \times 10^{-17}$, $\gamma = 9.07$, and $h_{-1} = 7.11 \times 10^{-17}$. The amplitude of the Lorentzian noise term is smaller than the fitted parameter from the measurement shown in Figure 4.5. The result implies a less significant effect of a single dominant

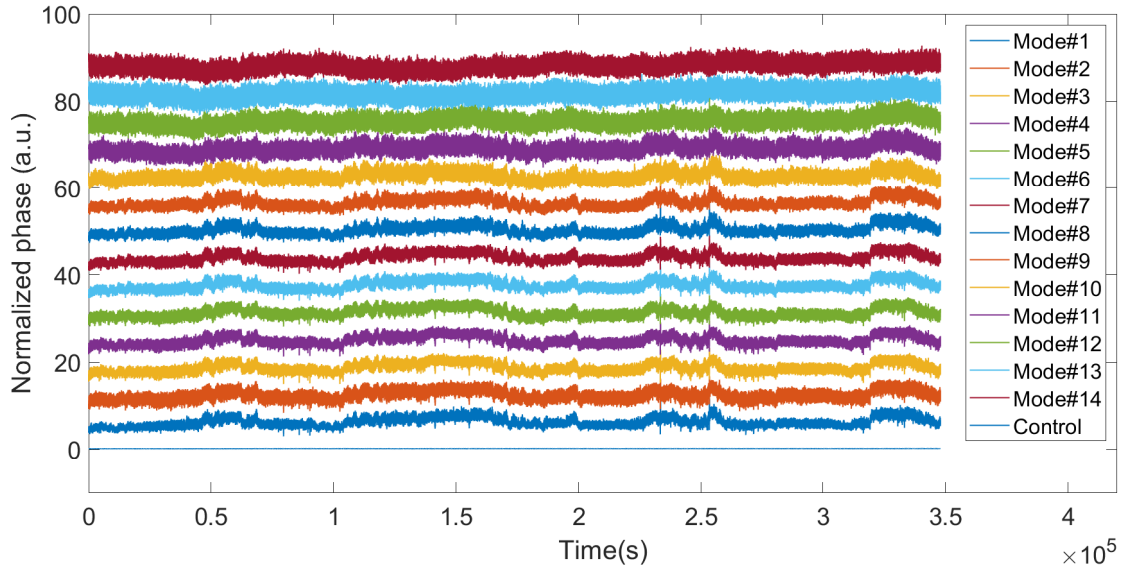


Figure C.2: The time traces of the measured phases. The bottom trace represents the control tone measured at 2.39 GHz, which is off-resonance with the SAW modes.

TLS, which is consistent with the PSD plot.

The correlation between the measured amplitudes and phases are illustrated in Figure C.5. The resonance frequency shifts are computed and the correlation coefficients are determined. Figure C.6 shows that the correlation coefficients diminishes as a function of the frequency detuning, which conforms to the results obtained from the shorter measurement discussed in Chapter 4.

The magnitude-squared coherence plots between the resonance frequency fluctuation between mode #1 and the other modes exhibit the different variations from the lowest frequency up to 10^{-1} Hz, which corresponds to the correlation coefficients shown in Figure C.6.

C.2 Single-mode measurement

This section describes a single resonance mode measurement, where 31 probing frequencies are positioned within one particular resonance mode, at 2.381 GHz. The positions of the probing frequencies are demonstrated in Figure C.8. The control tone is placed outside the resonance line shape, at 2.39 GHz.

Subsequently, the correlation coefficients of the amplitudes and phases are computed. The results are illustrated in Figure C.9. The resonance frequency shifts are calculated. The correlation matrix is shown in Figure C.10. Suppose that the optimal probing frequency for observing resonance frequency shift is at f_r , the tones that show high correlation with the tone at f_r indicate that they are fairly sensitive to the TLS noise. Hence, it is plausible to observe the resonance frequency fluctuations if the probing tones slightly deviate from f_r .

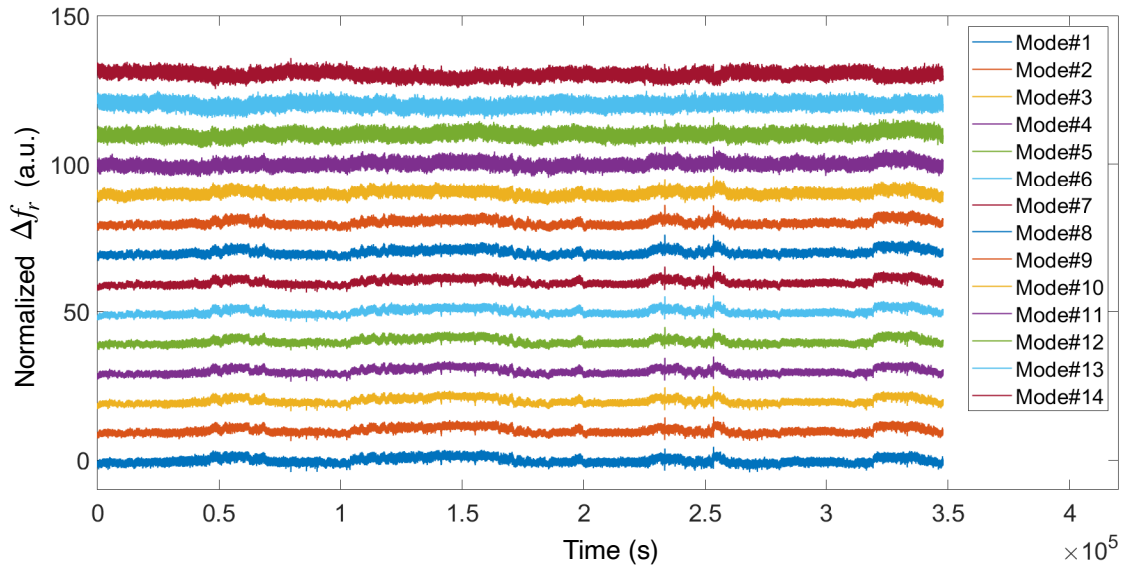


Figure C.3: The time trace of the calculated resonance frequency shifts. Note that there is no converted frequency from the control tone because it does not correspond to any resonance mode.

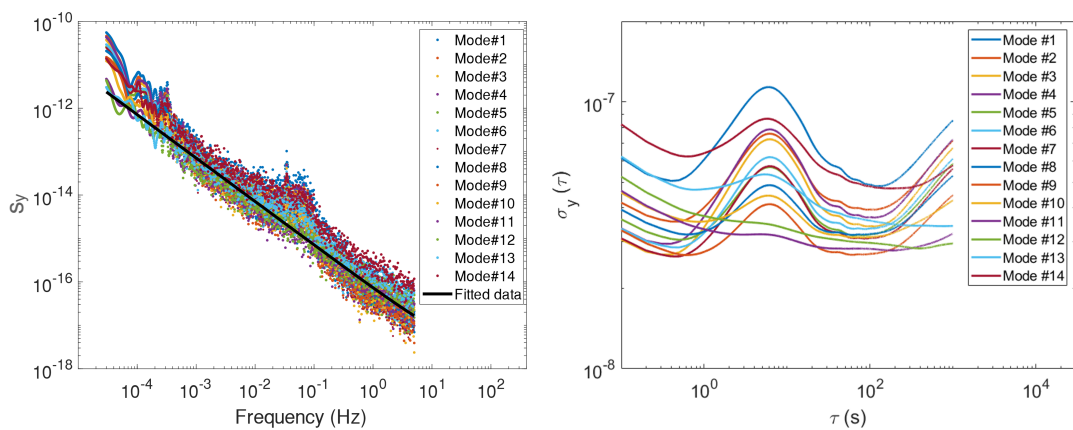


Figure C.4: (Left) Welch power spectral density and (right) Allan deviation of the resonance frequency shifts.

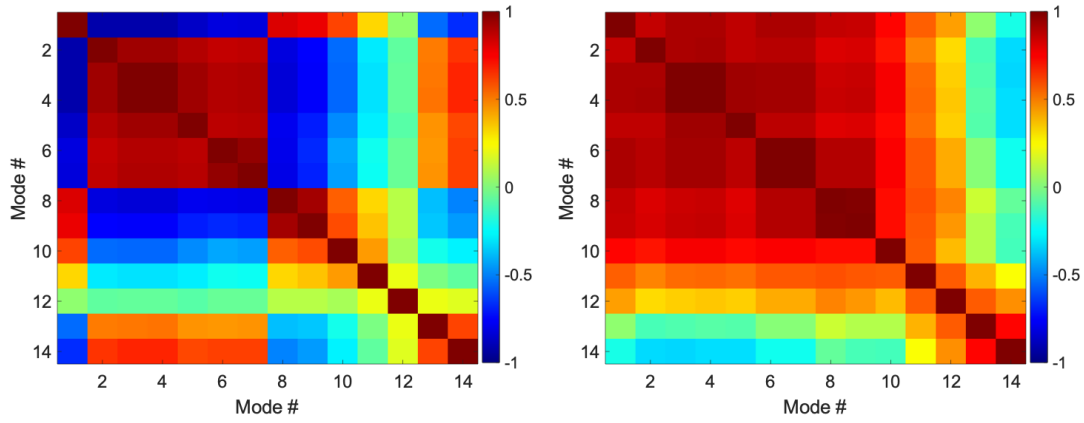


Figure C.5: The correlation matrices of (left) the amplitudes and (right) the phases of the data.

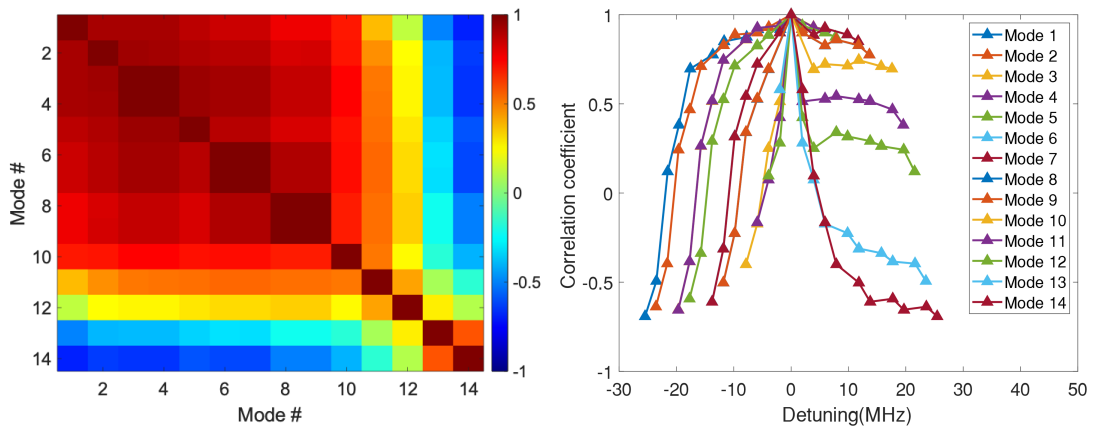


Figure C.6: (Left) the correlation matrices of the resonance frequency shifts and (right) the plot showing correlation coefficients as a function of detuning.

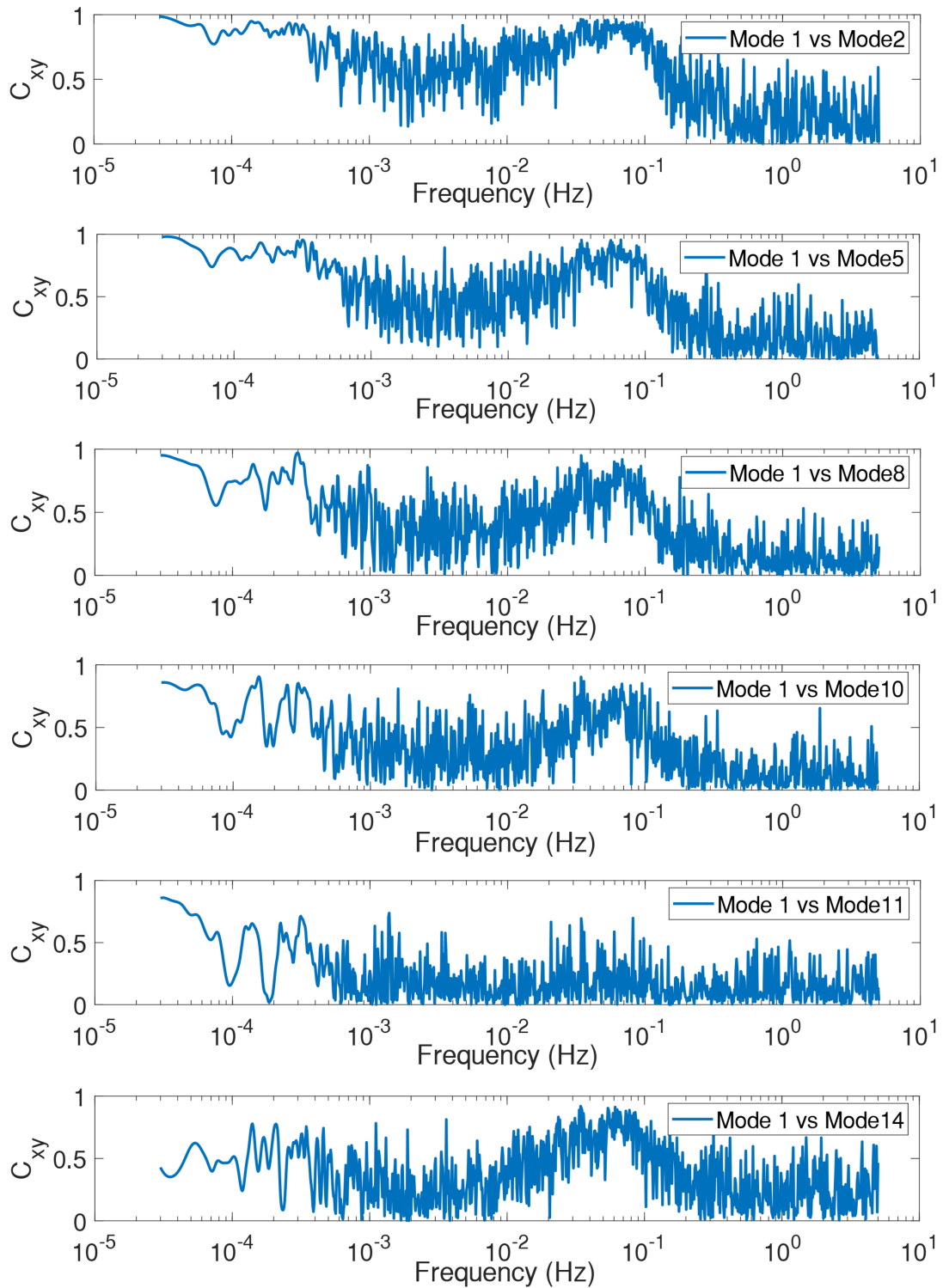


Figure C.7: Magnitude-squared coherence of the resonance frequency shifts between mode #1 and the others.

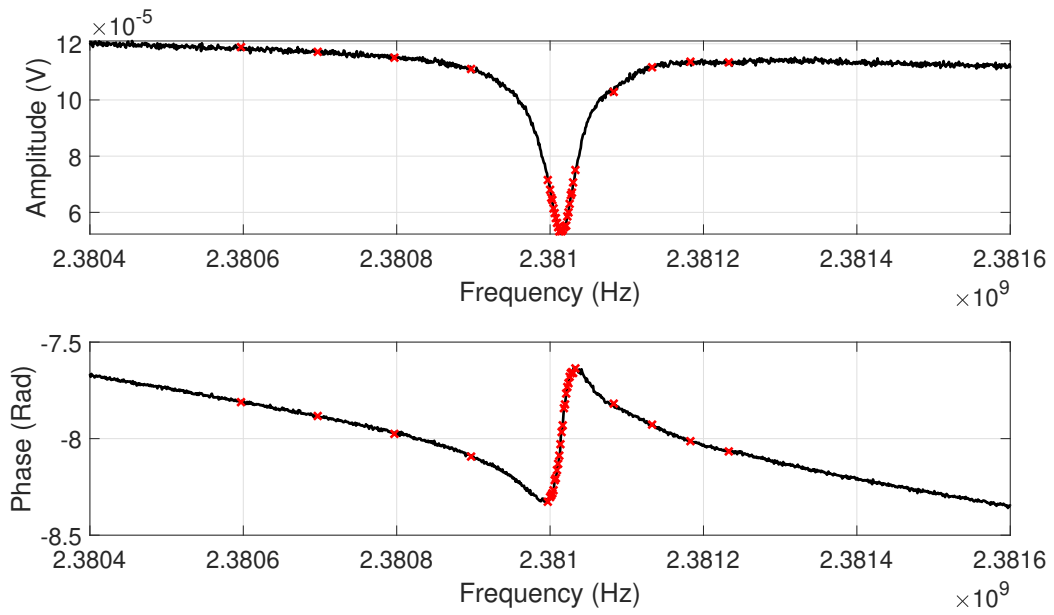


Figure C.8: The probing frequencies driven in a single mode measurement.

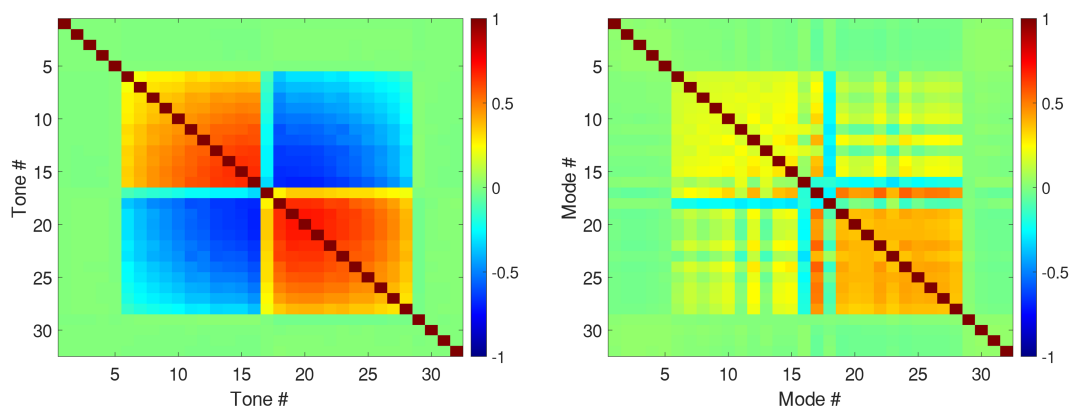


Figure C.9: The matrices showing correlation coefficients of (left) the amplitudes and (right) the phases of the single mode measurement.

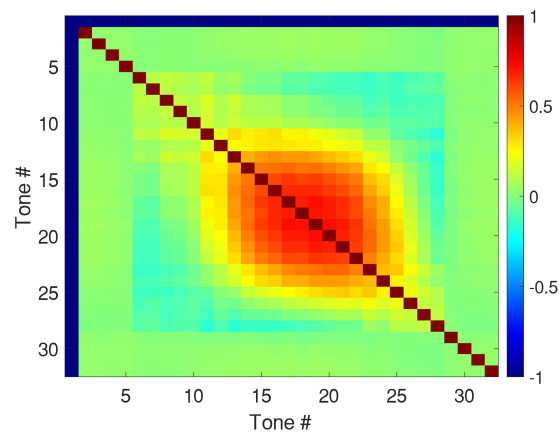


Figure C.10: The matrices showing correlation coefficients of the resonance frequency shifts calculated from the single mode measurement.